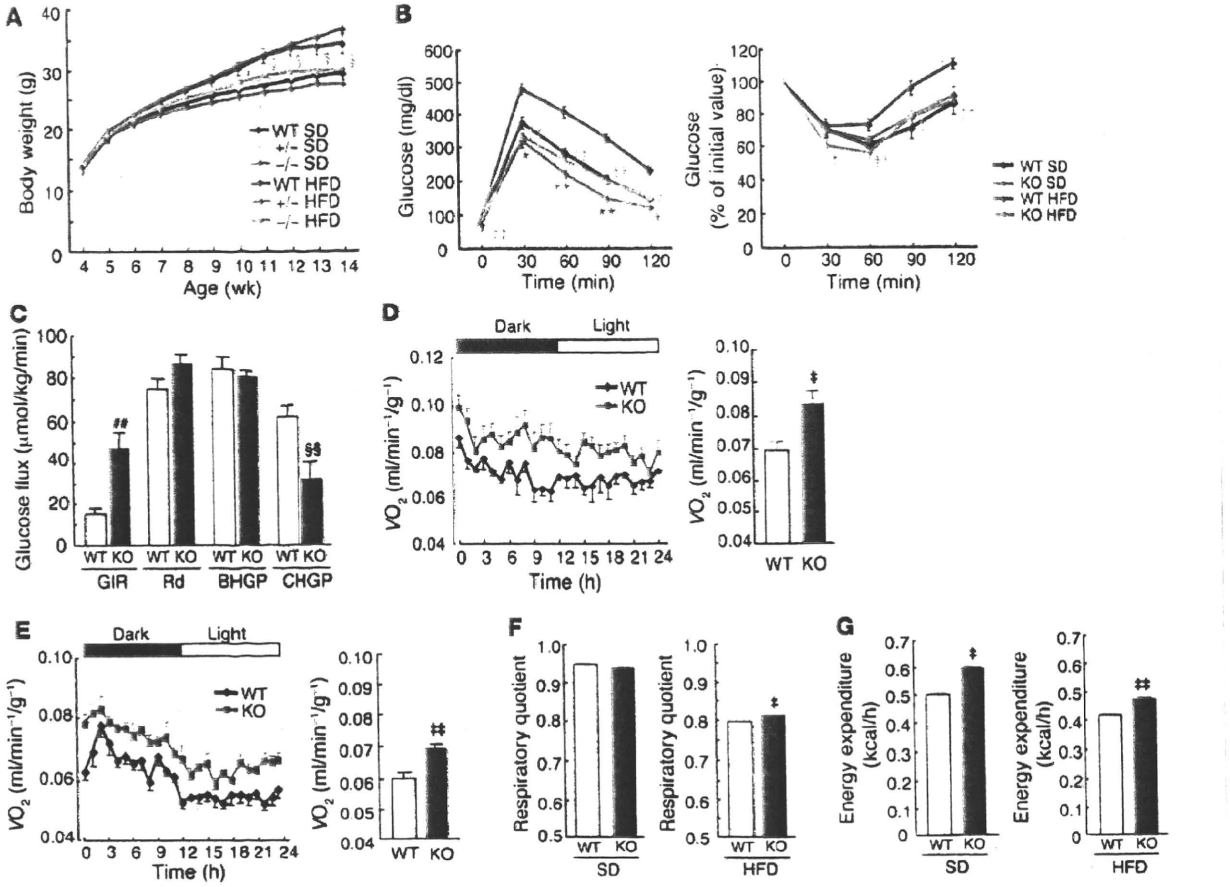

Figure 2

Glucose and energy metabolism in FSP27-knockout mice. (**A**) Body weight of wild-type, FSP27 heterozygous knockout (+/–), and FSP27-KO (–/–) mice maintained on a standard diet (SD) or fed a high-fat diet (HFD). Data are mean ± SEM (n = 7–11). $^{\S}P < 0.05$ versus corresponding values for wild-type or FSP27 heterozygous knockout mice on the high-fat diet; $^{*}P < 0.05$ versus corresponding value for FSP27 heterozygous knockout mice on the high-fat diet. (**B**) Plasma glucose concentrations during an intraperitoneal glucose tolerance test (left panel) or an insulin tolerance test (right panel) in 12-week-old wild-type and FSP27-KO (KO) mice, either maintained on a standard diet or fed a high-fat diet from 4 weeks of age. Data are mean ± SEM (n = 11 for standard diet; n = 8 for high-fat diet.). $^{*}P < 0.05$, $^{**}P < 0.01$ versus corresponding value for wild-type animals on the standard diet; $^{\dagger}P < 0.05$, $^{\dagger\dagger}P < 0.01$ versus corresponding value for wild-type animals on the high-fat diet. (**C**) Hyperinsulinemic-euglycemic clamp analysis in 10- to 12-week-old wild-type and FSP27-KO mice fed a high-fat diet. GIR, glucose infusion rate; Rd, rate of glucose disappearance; BHGP, basal hepatic glucose production; CHGP, hepatic glucose production during the clamp period. Data are mean ± SEM (n = 6). $^{\S\S}P < 0.05$, $^{\#\#}P < 0.01$ versus corresponding value for wild type. (**D** and **E**) Whole-body oxygen consumption rate (VO_2, expressed in milliliters per minute per gram of body weight) during a 12-hour dark/12-hour light cycle in 12-week-old mice fed a standard diet (n = 3 for wild type; n = 5 for FSP27-KO) (**D**) or a high-fat diet (n = 6) (**E**) is shown in the left panels. The average values for the 24-hour period are shown in the right panels. Data are mean ± SEM. $^{\ddagger}P < 0.05$, $^{\ddagger\ddagger}P < 0.01$ versus wild type. (**F** and **G**) Average values of respiratory quotient (VCO_2/VO_2) (**F**) and energy expenditure (**G**) for the 24-hour period in the experiments shown in **D** and **E**. Data are mean ± SEM. $^{\ddagger}P < 0.05$, $^{\ddagger\ddagger}P < 0.01$ versus wild type.

Multilocular lipid droplet formation as well as enhanced mitochondrial biogenesis and glucose and FFA oxidation in WAT of FSP27-KO mice. To investigate the mechanism responsible for the increased oxygen consumption and energy expenditure of FSP27-KO mice, we examined adipose tissue of these animals. The amounts of epididymal and subcutaneous WAT, but not those of BAT, were reduced in FSP27-KO mice compared with those in wild-type mice (Figure 3A). Furthermore, epididymal WAT of FSP27-KO mice was a brownish color similar to that of BAT (Figure 3A). A high-fat diet increased the amounts of epididymal and subcutaneous WAT to a greater extent in wild-type mice than in FSP27-KO mice (Supplemental Figure 8). The weight and appearance of adipose tissue of FSP27 heterozygous knockout mice were similar to those for wild-type mice (data not shown). Both subcutaneous and epididymal white adipocytes of FSP27-KO mice accumulated multilocular fat droplets (Figure 3B and Supplemental Figure 9). The size of lipid droplets in BAT of FSP27-KO mice also appeared to be increased (Figure 3B and Supplemental Figure 9). Transmission electron microscopy confirmed that lipid droplets in subcutaneous white adipocytes of FSP27-KO mice are multilocular and smaller than those of wild-type mice (Figure 3C). It also revealed that the number of mitochondria per cell in WAT of FSP27-KO mice was twice

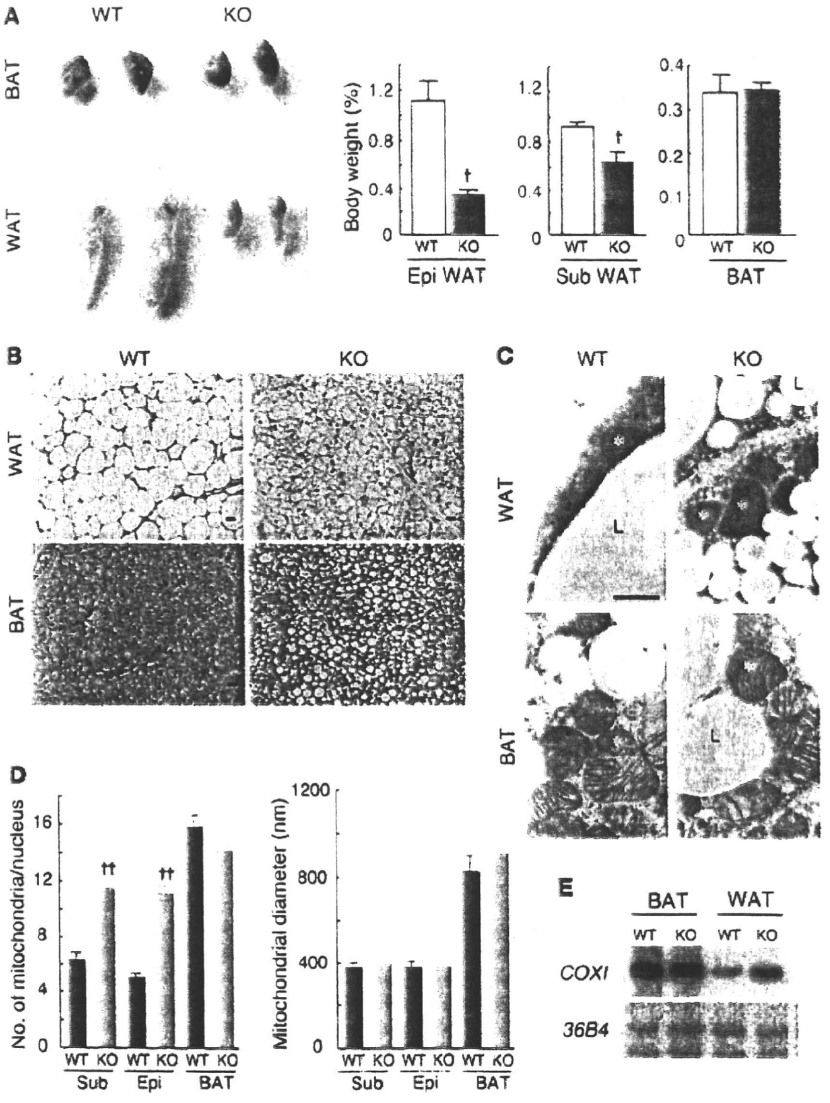

Figure 3
Characterization of adipose tissue in FSP27 knockout mice. (**A**) Comparison of interscapular brown fat pads (BAT) and epididymal white fat pads (WAT) of 14-week-old wild-type and FSP27-KO mice (left panel). Weights of epididymal WAT, subcutaneous WAT, and BAT isolated from 14-week-old wild-type and FSP27-KO mice (right panels). Data are mean ± SEM (n = 4–8). $^{\dagger}P < 0.05$ versus the corresponding value for wild type. (**B**) Sections of subcutaneous WAT and interscapular BAT from 14-week-old wild-type and FSP27-KO mice were stained with hematoxylin-eosin and examined by light microscopy. Scale bar: 20 μm. (**C**) Transmission electron microscopy of subcutaneous WAT and interscapular BAT from 6-week-old wild-type and FSP27-KO mice. L, lipid droplet; *, mitochondria. Scale bar: 500 nm. (**D**) Mitochondrial number (left panel) and size (right panel) in subcutaneous WAT, epididymal WAT, and interscapular BAT determined from electron micrographs similar to those in **C**. Mitochondrial number is expressed per nucleus and was determined for 25 wild-type and 28 FSP27-KO cells for subcutaneous WAT, 33 cells for epididymal WAT, and 56 wild-type and 64 FSP27-KO cells for BAT. Mitochondrial diameter was measured with a scale of 25 nm in 120 cells. Data are mean ± SEM. $^{\dagger\dagger}P < 0.01$ versus the corresponding value for wild type. (**E**) Southern blot analysis of total cellular DNA from BAT or WAT of 9-week-old wild-type or FSP27-KO mice with probes specific for the mitochondrial *COXI* gene and the nuclear *36B4* gene.

that in wild-type mice, although the size of these organelles did not differ between the 2 genotypes (Figure 3, C and D). In addition, Southern blot analysis with a probe specific for the mitochondrial gene for subunit I of cytochrome c oxidase (COXI) showed that the amount of mitochondrial DNA was increased in WAT of FSP27-KO mice (Figure 3E). No difference in mitochondrial number or size in BAT was apparent between FSP27-KO and wild-type mice (Figure 3, C and D). These results thus showed that mitochondrial biogenesis is substantially increased in WAT of FSP27-KO mice.

We next examined the abundance in adipose tissue of mRNAs for nuclear respiratory factor 1 (*NRF1*) and mitochondrial transcription factor A (*mtTFA*), both of which are transcription factors that play an important role in mitochondrial biogenesis (17, 18). RT-PCR analysis revealed that the amount of *NRF1* mRNA in WAT was significantly increased in FSP27-KO mice, reaching a level similar to that apparent in BAT of wild-type animals (Figure 4A). The amount of *mtTFA* mRNA in WAT was also increased significantly in FSP27-KO mice (Figure 4A). In addition, the amounts of mRNAs for PPARγ coactivator 1α (*PGC1a*) and *PGC1b*, important regulators of mitochondrial thermogenesis and biogenesis (19), were significantly increased in WAT of FSP27-KO mice, but these increased levels remained much smaller than those in BAT (Figure 4A). We also examined the abundance of mRNAs for acyl-CoA dehydrogenases, which are important for fatty acid oxidation in mitochondria. The amounts of mRNAs for very long-chain acyl-CoA dehydrogenase (*VLCAD*), long-chain acyl-CoA dehydrogenase (*LCAD*), and medium-chain acyl-CoA dehydrogenase (*MCAD*) were increased in WAT of FSP27-KO mice (Figure 4B). Furthermore, the amounts of mRNAs for *COXI*, *COXII*, and *COXIV*, all of which are components of COX and important for electron transport in mitochondria, were substantially increased in WAT of FSP27-KO mice (Figure 4C). However, the mRNA for uncoupling protein-1 (*UCP1*) was almost undetectable in WAT of FSP27-KO mice in contrast to its abundance in BAT (Figure 4C). These results thus suggested that the increase in mitochondrial mass in WAT of FSP27-KO mice is accompanied by an increase in FFA oxidation and subsequent oxidative phosphorylation but not by increased uncoupling or thermogenesis. To exclude a possible contribution of the liver and

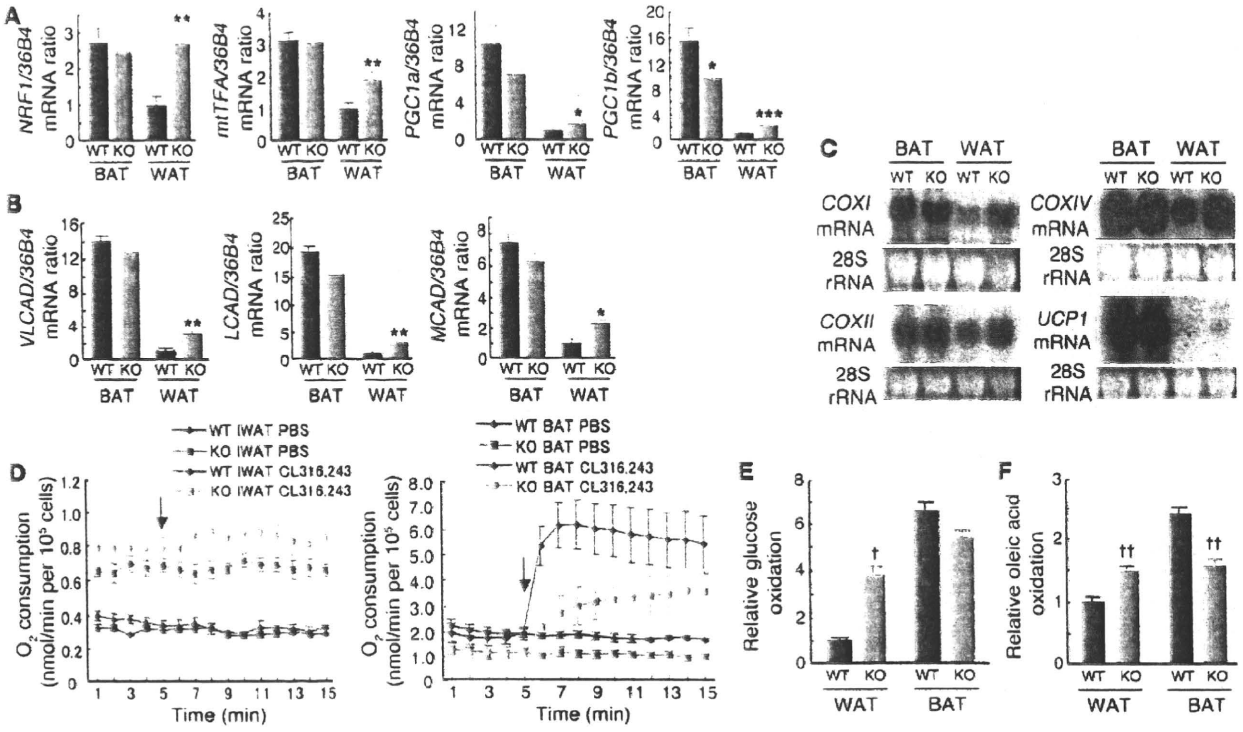

Figure 4

Mitochondrion-related gene expression and metabolic rate in WAT of FSP27-knockout mice. (**A** and **B**) Quantitative RT-PCR analysis of the expression of genes related to mitochondrial biogenesis (**A**) or to FFA oxidation (**B**) in WAT and BAT of 20-week-old wild-type and FSP27-KO mice. Data were normalized by the amount of *36B4* mRNA and expressed relative to the corresponding value for WAT of wild-type mice; data are mean ± SEM (n = 4). $^*P < 0.05$, $^{**}P < 0.01$, $^{***}P < 0.001$ versus the corresponding value for wild-type mice. (**C**) Northern blot analysis of mRNAs for *COXI*, *COXII*, *COXIV*, and *UCP1* in WAT and BAT of 14-week-old wild-type and FSP27-KO mice. (**D**) Oxygen consumption by adipocytes isolated from inguinal WAT (IWAT; left panel) or interscapular BAT (right panel) of wild-type and FSP27-KO mice. Arrows indicate the addition of the β_3-adrenergic agonist CL316,243 or vehicle (Ca^{2+}- and Mg^{2+}-free PBS). Data are mean ± SEM of values from 4 independent experiments. (**E** and **F**) Glucose (**E**) and oleic acid (**F**) oxidation in adipocytes isolated from epididymal WAT or interscapular BAT of wild-type and FSP27-KO mice. Data are expressed relative to the corresponding value for WAT of wild-type mice and are mean ± SEM of values from 4 WT or 3 KO independent experiments. $^{\dagger}P < 0.05$, $^{\dagger\dagger}P < 0.01$ versus the corresponding value for wild-type cells.

skeletal muscle to the increased oxygen consumption observed in FSP27-KO mice, we examined the abundance of mRNAs for carnitine palmitoyltransferase-1 (*CPT1*) and acyl-CoA dehydrogenases (*VLCAD*, *LCAD*, and *MCAD*) in these tissues by RT-PCR analysis and found no significant differences between FSP27-KO and wild-type mice (data not shown). In addition, there were no substantial differences between wild-type and FSP27-KO mice in the extent of lipid droplet accumulation as revealed by staining of TAG with oil red O in the liver or skeletal muscle (Supplemental Figure 10).

We also examined urinary catecholamines in FSP27-KO mice in order to evaluate the extent of systemic sympathetic activation, given that systemic β-adrenergic stimulation in mice and rats results in fragmentation of large lipid storage droplets and induction of mitochondrial biogenesis in WAT as well as upregulation of genes involved in fatty acid oxidation and mitochondrial electron transport in this tissue (20, 21). However, we found no significant differences in the amounts of urinary catecholamines (mean ± SEM) collected over a period of 72 hours between wild-type (n = 3) and FSP27-KO (n = 4) mice (adrenaline, 84.7 ± 10.3 versus 73.5 ± 6.5 ng, respectively; noradrenaline, 1,275.6 ± 36.1 versus 1,234.4 ± 168.5 ng, respectively; dopamine, 2,966.3 ± 212.3 versus 2,063.8 ± 299.4 ng, respectively), suggesting that the changes in WAT of FSP27-KO mice are not attributable to sympathetic β-adrenergic stimulation.

To examine directly the possible role of FSP27 in mitochondrial function in adipocytes, we first measured oxygen consumption of such cells isolated from FSP27-KO and wild-type mice. Consistent with the increased number of mitochondria in white adipocytes of FSP27-KO mice, the basal oxygen consumption of these cells was about twice that of cells from wild-type mice (Figure 4D). However, the β_3-adrenergic agonist CL316,243 did not substantially increase oxygen consumption in white adipocytes of wild-type or FSP27-KO mice (Figure 4D). In addition, the uncoupled respiration ratio for white adipocytes in the basal state did not differ between wild-type and FSP27-KO mice (Supplemental Figure 11), possibly reflecting the low abundance of *UCP1* mRNA in white adipocytes of both genotypes (Figure 4C). These results showed that mitochondrial function is upregulated in WAT of FSP27-KO mice, suggesting that the increased energy expenditure of these animals is attributable to increased mitochondrial biogenesis and function in WAT. In contrast to its lack of effect in WAT, CL316,243 induced a marked increase in oxygen consumption by adipocytes isolated from BAT of FSP27-KO or wild-type

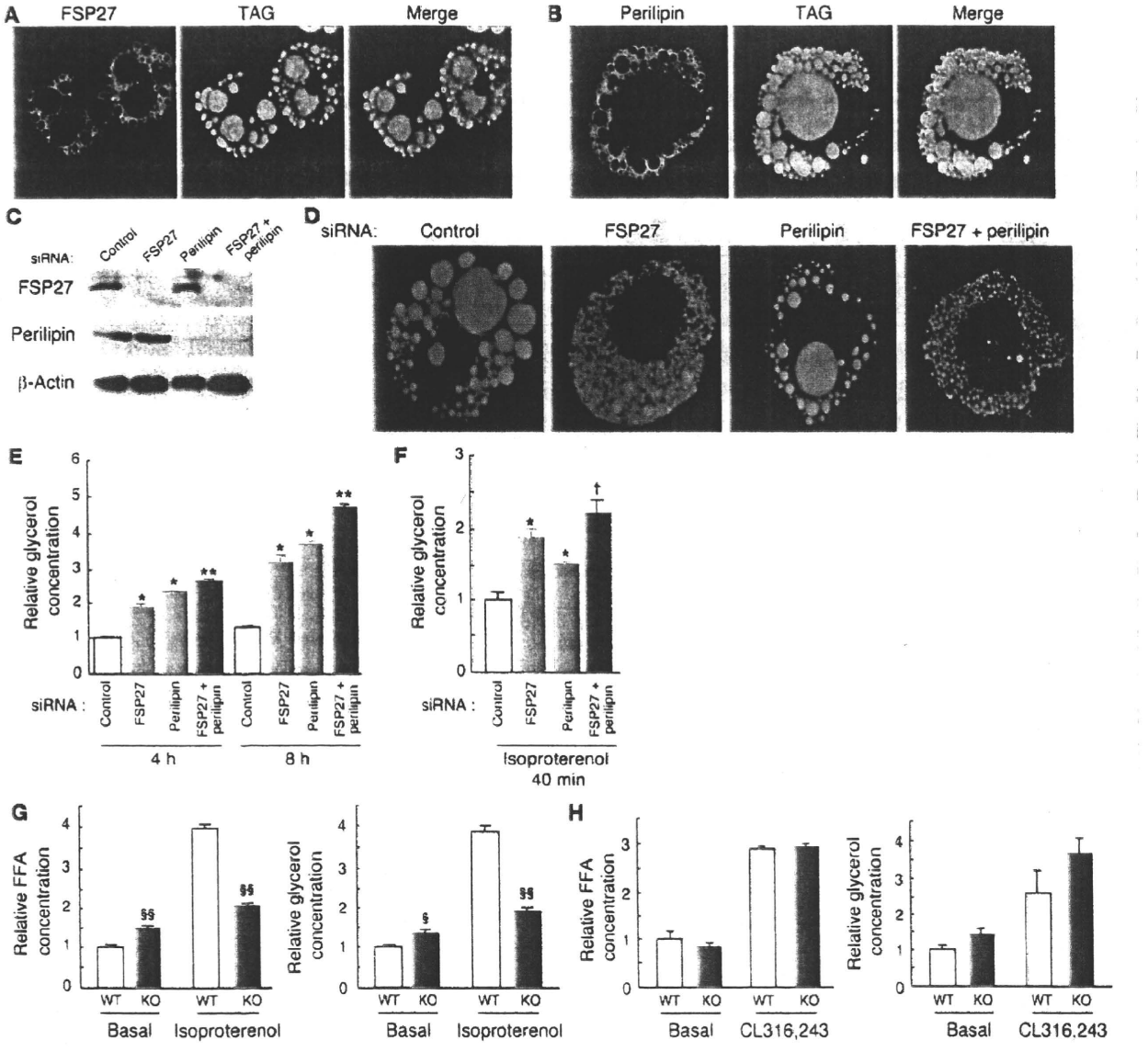

Figure 5

Localization of FSP27 to lipid droplets and its role in the pattern of lipid droplet accumulation in HW adipocytes. (**A** and **B**) Immunofluorescence localization of FSP27 (**A**) and perilipin (**B**) in HW adipocytes by confocal laser microscopy. TAG was stained with Bodipy 493/503. (**C**) Immunoblot analysis of FSP27, perilipin, and β-actin (control) in HW adipocytes 2 days after the introduction of FSP27 or perilipin siRNAs as indicated. (**D**) Pattern of lipid droplet accumulation in HW adipocytes 2 days after siRNA introduction as in **C**. TAG was stained with Bodipy 493/503. (**E**) Glycerol release of HW adipocytes during incubation for 4 or 8 hours, 2 days after introduction of siRNAs as in **C**. Data are mean ± SEM ($n = 6$) and are expressed relative to the value for control cells incubated for 4 hours. $^{*}P < 0.01$ versus corresponding value for control siRNA; $^{**}P < 0.01$ versus corresponding value for FSP27 or perilipin siRNA. (**F**) Glycerol release of HW adipocytes during incubation for 40 minutes with 10 μM isoproterenol 2 days after introduction of siRNAs as in **C**. Data are mean ± SEM ($n = 5$) and are expressed relative to the value for control cells. $^{*}P < 0.01$ versus corresponding value for control siRNA; $^{\dagger}P < 0.01$ versus corresponding value for perilipin siRNA. (**G**) Isolated white adipocytes of wild-type or FSP27-KO mice were incubated for 60 minutes in the absence (basal) or presence of 10 μM isoproterenol, after which concentrations of FFAs (left panel) and glycerol (right panel) in the culture medium were measured. Data are mean ± SEM ($n = 5$ WT or 4 KO for FFAs; $n = 4$ for glycerol) and are expressed relative to the corresponding basal value for wild-type cells. $^{\S}P < 0.05$, $^{\S\S}P < 0.01$ versus corresponding value for wild type. (**H**) Serum FFA (left panel) and glycerol (right panel) concentrations in wild-type and FSP27-KO mice measured 20 minutes after intraperitoneal injection of CL316,243 (0.1 mg/kg) or vehicle. Data are mean ± SEM ($n = 4$ WT or 3 KO) and are expressed relative to the corresponding basal value for wild-type mice. Original magnification, ×630.

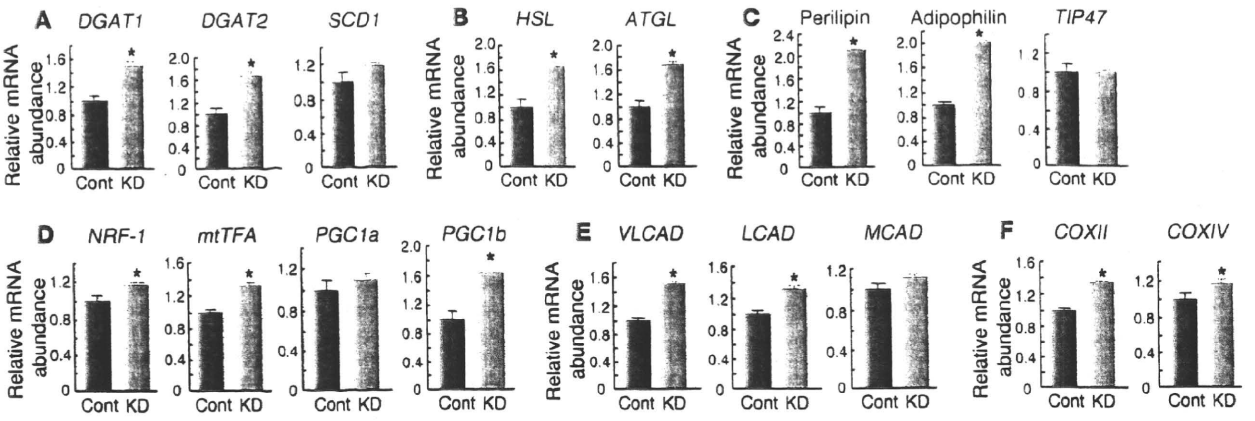

Figure 6

Effects of FSP27 depletion for 4 days on gene expression in HW adipocytes. Quantitative RT-PCR analysis of the expression of genes whose products are associated with lipid synthesis (**A**), lipolysis (**B**), lipid droplets (**C**), mitochondrial biogenesis (**D**), fatty acid oxidation (**E**), or oxidative phosphorylation (**F**) in HW adipocytes 4 days after the introduction of FSP27 siRNA (KD). Data were normalized by the amount of *36B4* mRNA and expressed relative to the corresponding value for control cells; they are mean ± SEM from 4 independent experiments. Cont, control. $^*P < 0.01$ versus control.

mice (Figure 4D). However, both basal and CL316,243-stimulated oxygen consumption were reduced by approximately 50% in brown adipocytes of FSP27-KO mice compared with those apparent for wild-type cells (Figure 4D). To examine further the role of FSP27 in mitochondrial function, we measured glucose and FFA oxidation in isolated adipocytes. Glucose and oleic acid oxidation were both increased in white adipocytes of FSP27-KO mice (Figure 4, E and F), consistent with the notion that mitochondrial function is upregulated in these cells. In contrast, oleic acid oxidation was decreased in brown adipocytes of FSP27-KO mice (Figure 4F). The findings that oxygen consumption and FFA oxidation were both decreased in brown adipocytes of FSP27-KO mice may be related to the increased size of lipid droplets in BAT of these animals (Figure 3B). Given that FSP27 was virtually undetectable in BAT of wild-type mice (Figure 1D), these changes observed in BAT of FSP27-KO mice may represent a compensatory response to the increased energy expenditure in WAT.

Ablation of FSP27 results in formation of multiple small lipid droplets, enhanced lipolysis, and depletion of TAG in HW adipocytes. Immunofluorescence microscopy with antibodies to FSP27 revealed that FSP27 was distributed in a ring around the lipid droplets of HW adipocytes (Figure 5A), suggesting that FSP27 localizes to the surface of these droplets. We also examined the distribution of perilipin, which is localized almost exclusively at the surface of lipid droplets in fat cells and steroidogenic cells and which inhibits lipolysis by blocking the access of lipases to the droplets (22–24). Perilipin was also localized to the surface of lipid droplets in HW adipocytes (Figure 5B), showing a distribution pattern similar to that of FSP27.

We next examined the effect of depletion of FSP27 by RNAi on lipid droplet formation in HW adipocytes. Introduction of an siRNA specific for *FSP27* mRNA into differentiated HW adipocytes resulted in the almost complete loss of FSP27 within 2 days (Figure 5C). This depletion of FSP27 resulted in the formation of numerous small lipid droplets in HW adipocytes, in contrast to the fewer and larger lipid droplets observed in control cells (Figure 5D). Quantitative analysis confirmed that depletion of FSP27 in HW adipocytes for 2 days resulted in an increase in lipid droplet number and a decrease in the mean area of individual droplets per cell (Supplemental Figure 12). Cells depleted of perilipin (Figure 5C) still manifested large lipid droplets, although all lipid droplets in such cells were generally smaller than those in control cells (Figure 5D). Cells depleted of both FSP27 and perilipin (Figure 5C) exhibited a pattern of lipid droplet formation similar to that observed in cells depleted of FSP27 alone (Figure 5D). The intracellular TAG content of HW adipocytes was significantly reduced 3 days after the introduction of FSP27 or perilipin siRNAs, and the effects of the 2 siRNAs appeared to be additive (Supplemental Figure 13). Measurement of glycerol released into the medium during culture of cells under basal conditions for 4 or 8 hours revealed that the extent of lipolysis was significantly increased in FSP27-depleted HW adipocytes compared with that apparent in control adipocytes at both time points (Figure 5E). Consistent with previous observations (25, 26), depletion of perilipin also increased the extent of basal lipolysis in HW adipocytes (Figure 5E). Depletion of both FSP27 and perilipin again increased basal lipolysis to a greater extent than did that of either protein alone. Examination of lipolysis in response to β-adrenergic stimulation revealed that depletion of FSP27 and perilipin also potentiated isoproterenol-induced lipolysis in an approximately additive manner (Figure 5F). These results suggested that FSP27 is important for the formation of large lipid droplets and that the loss of FSP27 promotes lipolysis and the consequent depletion of intracellular TAG by a mechanism distinct from that by which loss of perilipin induces this same effect.

To address further the function of FSP27 in lipolysis, we investigated the effect of FSP27 depletion on lipolysis both in isolated mouse adipocytes and in mice. We evaluated lipolysis in isolated adipocytes by measuring FFA and glycerol concentrations of the culture medium. Basal lipolysis was increased in isolated white adipocytes from FSP27-KO mice, although isoproterenol-stimulated lipolysis was impaired in these cells compared with that in white adipocytes from wild-type mice (Figure 5G). We next administered CL316,243 to mice and measured the products of lipolysis, FFAs

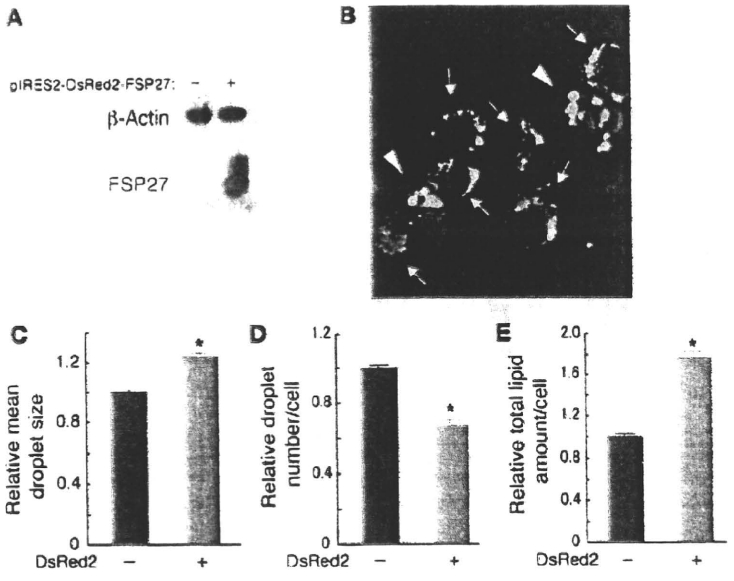

Figure 7
Formation of large lipid droplets induced by forced expression of FSP27 in COS cells. (**A**) Immunoblot analysis of FSP27 and β-actin (loading control) in COS cells 2 days after transfection with an expression plasmid encoding both FSP27 and DsRed2 (pIRES2-DsRed2-FSP27). (**B**) COS cells transfected with pIRES2-DsRed2-FSP27 as in **A** were incubated with 400 μM oleic acid for 24 hours and then stained with Bodipy 493/503 (for TAG). A merged image of Bodipy 493/503 and DsRed2 fluorescence is shown. Arrowheads and arrows indicate cells positive or negative for FSP27 expression, respectively. Original magnification, ×630. (**C–E**) Quantitation of mean droplet size (**C**), droplet number (**D**), and total lipid amount (**E**) per cell for COS cells treated as in **B** but also stained with Hoechst 33258 (for nuclei). Total lipid amount was calculated as the product of the area and green fluorescence density of each droplet per cell. Data are mean ± SEM of values from 1,502 and 444 cells negative or positive for DsRed2 fluorescence, respectively, and are expressed relative to the corresponding value for DsRed2-negative cells. *$P < 0.001$ versus DsRed2-negative cells.

and glycerol, in serum. Serum FFA and glycerol concentrations were similar in wild-type and FSP27-KO mice under basal or CL316,243-stimulated conditions (Figure 5H). These results differed from those previously obtained with perilipin-knockout mice, in which lipolysis stimulated by a β-adrenergic agonist in vivo was decreased compared with that in wild-type mice (25). The physiological role of FSP27 in mice may thus differ from that of perilipin.

We next examined the effects of FSP27 ablation on gene expression in HW adipocytes at both 2 and 4 days after the introduction of FSP27 siRNA. We confirmed that FSP27 remained almost completely depleted 4 days after siRNA introduction (data not shown). As shown above, depletion of FSP27 for 2 days was sufficient to induce multilocularization of lipid droplets (Figure 5D) and to increase lipolysis (Figure 5, E and F). RT-PCR analysis performed 2 days after introduction of siRNA revealed that the amounts of mRNAs for diacylglycerol acyltransferase type 1 (*DGAT1*), *DGAT2*, and stearoyl-CoA desaturase 1 (*SCD1*), all of which participate in lipid synthesis (27–31), did not differ between FSP27-depleted and control HW adipocytes (data not shown). In addition, the amounts of mRNAs for hormone-sensitive lipase (*HSL*) and adipose triglyceride lipase (*ATGL*), both of which contribute to TAG hydrolysis in adipocytes (32), were not significantly different between the FSP27-depleted and control cells (data not shown). However, 4 days after the introduction of siRNA, the amounts of these various mRNAs, with the exception of that of *SCD1* mRNA, were all increased in the FSP27-depleted cells (Figure 6, A and B). The abundance of mRNAs for perilipin, adipophilin, and *TIP47*, all of which coat lipid droplets and are important in lipid metabolism (7, 33), was not affected by depletion of FSP27 for 2 days (data not shown), but the amounts of perilipin and adipophilin mRNAs were increased significantly after 4 days (Figure 6C). Finally, we examined the expression of genes related to mitochondrial biogenesis or oxidative phosphorylation. Depletion of FSP27 for 2 days did not affect the abundance of mRNAs for *NRF1*, *mtTFA*, *PGC1a*, *PGC1b*, or the acyl-CoA dehydrogenases (*VLCAD*, *LCAD*, *MCAD*) in HW adipocytes (data not shown). The abundance of *COXII* mRNA was significantly increased (~1.87-fold; $P < 0.008$) by FSP27 depletion for 2 days, whereas that of *COXIV* mRNA was unaffected (data not shown). However, depletion of FSP27 for 4 days resulted in increases in the amounts of these various mRNAs, with the exception of those of *PGC1a* and *MCAD* (Figure 6, D–F). These results thus suggested that the increased expression of genes involved in lipid metabolism, lipid coating, or mitochondrial biogenesis or function is not the cause of multilocularization of lipid droplets but may be the result of it.

Forced expression of FSP27 promotes formation of large lipid droplets in COS cells. To confirm the function of FSP27 in WAT, we transfected COS cells, which do not express endogenous FSP27, with a vector that encodes both FSP27 and the fluorescence marker DsRed2. The expression of FSP27 in the transfected cells was confirmed by immunoblot analysis (Figure 7A). Control COS cells accumulated multiple small lipid droplets in the cytoplasm during culture for 24 hours in the presence of 400 μM oleate. In contrast, COS cells expressing FSP27, which were identified by monitoring the fluorescence of DsRed2, accumulated large lipid droplets (Figure 7B). Quantitative analysis revealed that the mean area of individual droplets per cell was significantly increased (Figure 7C), whereas the droplet number per cell was significantly decreased (Figure 7D) in cells expressing FSP27 compared with that in control cells. In addition, the total amount of lipid per cell was significantly increased in cells expressing FSP27 (Figure 7E). These results thus indicated that FSP27 promotes the formation of large lipid droplets and, consequently, increases cellular lipid content.

Discussion

Obesity is a disorder of energy balance, in which excess energy accumulates in WAT in the form of TAG. In white adipocytes, TAG is stored in large, often solitary cytoplasmic organelles, known as lipid droplets. These droplets are composed of a core of TAG surrounded by a phospholipid monolayer, in which numerous proteins are embedded (5). To understand the pathogenesis of obesity, it is therefore essential to characterize the mechanism of lipid droplet formation and its regulation. We have now shown that FSP27 is expressed at the protein level mainly in WAT, is associ-

ated with the large unilocular lipid droplets of white adipocytes, and is indispensable for the formation or maintenance of these droplets. In contrast to WAT, BAT accumulates small multilocular lipid droplets, likely because FSP27 is almost undetectable in this tissue, even though its mRNA is present in amounts similar to those in WAT.

Mammalian lipid droplets are associated with a specific set of proteins that are members of the PAT (perilipin-ADRP-TIP47) domain family, which include perilipin, ADRP (or adipophilin), TIP47, and S3-12 (7, 8). Loss of perilipin results in constitutive lipolysis in adipocytes under basal conditions (25, 26). We also found that perilipin depletion increased lipolysis in HW adipocytes, but this effect was not accompanied by a pronounced change in the pattern of lipid droplet accumulation in contrast to the multilocularization of lipid droplets induced in these cells by depletion of FSP27. These results suggest that the lipolysis induced in HW adipocytes by depletion of FSP27 is mediated by a mechanism distinct from that by which perilipin depletion elicits this effect. The change in the pattern of lipid droplet accumulation induced by loss of FSP27 suggests that the accompanying increase in lipolysis may result from the multilocularization of large lipid droplets. Such multilocularization thus increases the total surface area of lipid droplets in a cell and thereby likely increases the access of lipases to stored lipid. Thus, multilocularization of lipid droplets can be the cause of the increased lipolytic rate in WAT lacking FSP27. Conversely, unilocular lipid droplets are thought to impede lipolysis by minimizing the accessibility of stored lipid to lipases and thereby to be important for efficient TAG storage in WAT. Acute and robust lipolysis of multilocular lipid droplets may be necessary for the efficient supply of FFAs to mitochondria in energy-consuming tissues such as BAT. Indeed, the small lipid droplets of BAT are surrounded by a large number of mitochondria, which are responsible for the uncoupled respiration of FFAs derived from lipid droplets (34). The pattern of intracellular lipid formation may therefore be closely related to the metabolic characteristics of cells.

FSP27-KO mice show a lean phenotype, increased metabolic rate, and resistance to diet-induced obesity. These characteristics likely result from the decreased TAG storage function, the increased mitochondrial biogenesis, and the increased energy expenditure in WAT of these animals. Depletion of FSP27 in HW adipocytes for 2 days resulted in the formation of multiple small lipid droplets and enhanced lipolysis, without an increase in the expression of genes involved in lipid metabolism or mitochondrial biogenesis or function. However, depletion of FSP27 for 4 days led to upregulation of the expression of such genes. These results suggest that the primary event induced by FSP27 depletion may indeed be the multilocularization of lipid droplets and the consequent increase in lipolysis. The increased mitochondrial biogenesis observed in WAT of FSP27-KO mice hence may be secondary to the increased lipolysis. The increased availability of FFAs and their metabolites may stimulate members of the PPAR family in WAT of FSP27-KO mice and thereby induce the secondary mitochondrial biogenesis. Indeed, several FFAs have been shown to stimulate PPARα and PPARδ (35). In addition, activation of PPARα and PPARγ has been shown to increase mitochondrial copy number as well as the expression of UCP-1, MCAD, and CPT-1 (36). Activation of PPARδ in adipose tissue also induces expression of genes required for FFA oxidation and energy expenditure (37). The increase in intracellular lipolysis in adipocytes can thus lead to increased mitochondrial biogenesis and FFA oxidation.

Perilipin-knockout mice are characterized by constitutive lipolysis. They have reduced adipose mass and are also resistant to diet-induced obesity (25, 26). These phenotypes are similar to those of FSP27-KO mice. The most prominent difference between these 2 mouse lines is the pattern of lipid droplet formation in WAT. The multilocular pattern of lipid droplet formation observed in WAT of FSP27-KO mice is thus not apparent in perilipin-knockout mice (25, 26). In addition, increased mitochondrial biogenesis was not apparent in WAT of the perilipin-knockout mice, at least not in histological analysis. Furthermore, perilipin-knockout mice show a tendency to develop insulin resistance (26, 38), despite increased β-oxidation in skeletal muscle, heart, and WAT (38, 39), that is thought to be an adaptive response to consume the FFAs generated by the increased rate of lipolysis in WAT. In contrast, FSP27-KO mice showed improved glucose tolerance and insulin sensitivity, without an apparent increase in β-oxidation in the liver or skeletal muscle. These results suggest that the FFAs generated by the increased lipolysis in WAT of FSP27-KO mice are efficiently oxidized by the increased number of mitochondria in WAT itself, without the need for compensation by the liver or skeletal muscle. The multilocular pattern of lipid droplet accumulation in WAT of FSP27-KO mice likely facilitates the efficient transfer of FFAs to the abundant neighboring mitochondria. These data suggest the mechanism by which increased lipolysis in WAT does not result in insulin resistance in FSP27-KO mice.

FSP27 belongs to the CIDE (cell death–inducing DFF45-like effector) family of proteins, which show sequence similarity to the NH_2-terminal region of the proapoptotic DNA fragmentation factor 40 (DFF40) and its inhibitor DFF45 (40). This family also includes CIDE-A and CIDE-B in addition to FSP27 (40). CIDE-A is expressed specifically in BAT in mice, and its deficiency in these animals results in resistance to diet-induced obesity as well as in upregulation of thermogenesis and metabolic rate through release of direct suppression of UCP-1 activity (41). CIDE-B is expressed predominantly in liver, and CIDE-B–knockout mice are resistant to diet-induced obesity and liver steatosis (42). FSP27 and CIDE-A may therefore play regulatory roles in mice for lipid storage in WAT and energy expenditure in BAT, respectively. In humans, however, *CIDEA* mRNA is present in WAT, and a low level of *CIDEA* gene expression in adipose tissue was associated with several features of metabolic syndrome (43). In addition, there are several similarities between human CIDE-A and mouse FSP27. Culture of human primary adipocytes with TNF-α thus resulted in a decrease in the amount of *CIDEA* mRNA, and depletion of CIDE-A from these cells by RNAi induced an increase in lipolysis (43). The human ortholog of mouse FSP27 has been identified, but the characteristics of this protein, including its expression in adipose tissue, were not examined (44). During the preparation of this manuscript, FSP27 was shown to enhance TAG storage in cultured cells (11). Further studies are necessary to characterize the functions of CIDE family proteins, especially in humans.

In summary, we have shown that FSP27 plays a physiologically important role in efficient energy storage in WAT, by promoting the formation of unilocular lipid droplets in this tissue. Such regulation of lipid droplet formation by FSP27 has pronounced effects on energy metabolism of the whole body. Our data suggest that alteration of the pattern of lipid droplet accumulation in white adipocytes by modulation of FSP27 function is a potential therapeutic strategy for treatment of obesity and its related disorders.

Methods

Oligonucleotide microarray analysis. Total RNA was prepared from 3T3-L1 cells that had been induced to differentiate into adipocytes as previously described (12) and then infected for 48 hours with an adenovirus encoding PPARγ-ΔC (12) or a control adenovirus at an MOI of 50 PFU per cell. RT, second-strand cDNA synthesis, and production of biotin-labeled cRNA were performed with 10 μg of total RNA as the initial template. The labeled cRNA was purified, fragmented, and subjected to hybridization with GeneChip mouse microarrays (Mu11K; Affymetrix). After washing and staining, the arrays were scanned with a Hewlett Packard confocal laser scanner and visualized with Affymetrix GeneChip 3.1 software. The data were analyzed with GeneChip Analysis Suite software version 4.0 (Affymetrix), and the fold differences in hybridization intensity between the two 3T3-L1 adipocyte samples were determined.

Generation of FSP27-knockout mice. We isolated *Fsp27* genomic clones from the female mouse 129s6/SvEvTAC Taconic BAC Library (Children's Hospital Oakland Research Institute, Oakland, California, USA) and prepared a targeting construct in which the *Fsp27* sequence between ApaI and XhoI sites, including the first and second exons, was replaced with the neomycin resistance gene (Supplemental Figure 5A). The targeting plasmid was linearized with NotI and introduced by electroporation into EB3/5 embryonic stem cells. Cell clones resistant to G418 and gancyclovir were isolated, and genomic DNA was extracted from these cells, digested with EcoRV, and subjected to Southern blot analysis in order to confirm homologous recombination (Supplemental Figure 5B). Two lines of chimeric mice were obtained by injection of cells from these clones into C57BL/6N blastocysts. Crossing of the chimeric mice with C57BL/6J mice yielded offspring that harbored the disrupted *Fsp27* allele in the germ line. FSP27-KO mice were obtained by breeding of heterozygotes. Immunoblot analysis did not detect FSP27 in WAT of FSP27-KO mice and revealed that the amount of this protein was reduced by approximately 50% in WAT of FSP27 heterozygous-knockout mice (Supplemental Figure 5C). For the experiments in the present study, we used male mice that had been backcrossed to the C57BL/6J background for more than 6 generations. Mice were maintained under a 12-hour light/12-hour dark cycle and had free access to food and water. In experiments examining the effects of a high-fat diet, mice were fed chow in which fat constituted 56% of calories (Oriental Yeast), beginning at 4 weeks of age. Mice were obtained from Japan SLC. Experimental protocols with mice were performed in accordance with the guidelines of the and with approval of the animal ethics committee of Kobe University Graduate School of Medicine.

Isolation of total RNA, northern blot analysis, and quantitation of mitochondrial DNA. Total RNA was extracted from various tissues and cells with the use of an RNeasy kit (QIAGEN) or the TRIzol reagent (Invitrogen), and portions (10 μg) of the isolated RNA were subjected to northern blot analysis. Probes were prepared by RT-PCR from total RNA extracted from 3T3-L1 adipocytes (for FSP27 and 36B4) or from mouse BAT (for COXI, COXII, COXIV, and UCP-1). The probes were labeled with ^{32}P with the use of a Rediprime II Random-Primer Labeling system (GE Healthcare). Autoradiograms of blots were visualized with a BAS2500 image analyzer (Fuji Film). Measurement of mitochondrial DNA was performed as described previously (45). In brief, cDNA probes for *COXI* and *36B4* genes were generated by RT-PCR from total RNA extracted from mouse BAT and were labeled with ^{32}P with the use of a Rediprime Random-Primer Labeling kit. Total DNA was extracted from mouse epididymal WAT or BAT, and portions (10 μg) of the DNA were digested with EcoRV and BglII. The resulting DNA fragments were fractionated by electrophoresis on a 0.7% agarose gel and then transferred overnight to a nylon membrane (HyBond N+; GE Healthcare). The membrane was incubated for 30 minutes at 65°C with Rapid-Hyb Hybridization buffer (GE Healthcare), subjected to hybridization with the radioactive probes overnight at 65°C, and then washed at 65°C twice for 30 minutes with 0.1× SSC containing 0.1% SDS. Autoradiograms of blots were visualized with a BAS2500 image analyzer.

Preparation of HB2 and HW cells and measurement of glycerol release and cellular TAG. HB2 and HW cells were prepared from interscapular BAT and epididymal WAT, respectively, of p53 homozygous knockout mice as described previously (16). The cells were maintained in DMEM (Sigma-Aldrich) supplemented with 10% FBS (JRH Biosciences), streptomycin (50 μg/ml), and penicillin (50 U/ml). At confluence, fresh medium supplemented with 0.5 mM 3-isobutyl-1-methylxanthine and 1 nM dexamethasone was added to the cells for induction of adipocyte differentiation. After 2 days, the medium was changed to DMEM supplemented with 50 nM triiodothyronine and insulin (10 μg/ml) and was refreshed every 2 days. The amount of glycerol released into culture medium by HW cells was determined with the use of a colorimetric assay (Sigma-Aldrich). The TAG content of isopropanol extracts prepared from HW cells grown in 12-well plates was determined with an acetyl acetone–based colorimetric assay kit (Wako)

Quantitative RT-PCR. Complementary DNA synthesized from total RNA was analyzed in a Sequence Detector (model 7900; PE Applied Biosystems) with specific primers and SYBR Green PCR Master reagents (Perkin Elmer Life Sciences). The relative abundance of mRNAs was calculated with *36B4* mRNA as the invariant control. The primers (sense and antisense, respectively) were as follows: *FSP27*, 5′-CTGGAGGAAGATGGCACAATCGTG-3′ and 5′-CAGCCAATAAAGTCCTGAGGGTTCA-3′; *mtTFA*, 5′-AGTTCCCACGCTGGTAGTGT-3′ and 5′-GCGCACATCTCGACCC-3′; *NRF1*, 5′-CAGCAACCCTGATGGCACCGTGTCG-3′ and 5′-GGCCTCTGATGCTTGCGTCGTCTGG-3′; *PGC1a*, 5′-GGAGCTGGATGGCTTGGGACAT-3′ and 5′-TTCGCAGGCTCATTGTTGTACTGGT-3′; *PGC1b*, 5′-GGCTCTTCCGCTCACA-3′ and 5′-ACCTGGCAGTAGTCGTGGTC-3′; *CPT1*, 5′-GCTGCTTCCCCTCACAAGTTCC-3′ and 5′-GCTTTGGCTGCCTGTGTCAGTATGC-3′; *VLCAD*, 5′-GAATGACCCTGCCAAGAACGA-3′ and 5′-ATGCCCACAATCTCTGCCAAG-3′; *LCAD*, 5′-GGACTCCGGTTCTGCTTCCA-3′ and 5′-TGCAATCGGGTACTCCCACA-3′; *MCAD*, 5′-CAACACTCGAAAGCGGCTCA-3′ and 5′-ACTTGCGGGCAGTTGCTTG-3′; *DGAT1*, 5′-ACCGCGAGTTCTACA-3′ and 5′-AGGGGAACGCTCACTAGGTA-3′; *DGAT2*, 5′-GCGCTACTTCCGAGACTACTTT-3′ and 5′-GCACAGGCATCCGGAAGTTACC-3′; *SCD1*, 5′-TCTCAGAAACACACGCCGACC-3′ and 5′-AGGCCGGGCTTGTAGTACCTC-3′; *HSL*, 5′-TGTGGCACAGACCTCTAAAT-3′ and 5′-GGCATATCCGCTCTC-3′; *ATGL*, 5′-GGAGACCAAGTGGAACATCTCA-3′ and 5′-AATAATGTTGGCACCTGCTTCA-3′; perilipin, 5′-TGCTGGATGGAGACCTC-3′ and 5′-ACCGGCTCCATGCTCCA-3′; adipophilin, 5′-AAGCATCGGCTACGACGACAC-3′ and 5′-GGACAGTCTGGCATGTAGTCTGGA-3′; *TIP47*, 5′-AGGACTTTGCAACTGCTGCTGA-3′ and 5′-AGGACTTTGCAACTGCTGCTGA-3′; *COXII*, 5′-GCCGACTAAATCAAGCAACAG-3′ and 5′-TCTAGGACAATGGGCATAAAGCTATTAA-3′; *COXIV*, 5′-AGCCATTTCTACTTCGGTGTG-3′ and 5′-GCAGACAGCATCGTGACAT-3′; and *36B4*, 5′-GAGGAATCAGATGAGGATATGGGA-3′ and 5′-AAGCAGGCTGACTTGGTTGC-3′.

Measurement of metabolic parameters. Plasma insulin concentration was measured with an insulin assay kit (Morinaga Institute of Biological Science). FFA and TAG concentrations in serum were measured with NEFA-C and Triglyceride E tests (Wako), respectively. Serum adiponectin and leptin levels were measured with ELISA kits from Otsuka Pharmaceutical and R&D Systems, respectively. Liver lipids were extracted from tissue homogenates with isopropanol, and the TAG content was determined with a Triglyceride E test. For intraperitoneal glucose tolerance tests, mice were deprived of food for 16 to 18 hours and then injected with glucose (2 g per kilogram of body mass). For intraperitoneal insulin tolerance tests, mice were injected with human regular insulin (0.75 U/kg; Eli Lilly). Blood samples were collected

before and after injections, and plasma glucose concentration was measured with a Glutestsensor (Sanwa Chemical). Food intake was measured by weighing the food given at the beginning and that remaining at the end of each day for 1 week. For catecholamine measurements, urine was collected in bottles containing HCl and subjected to HPLC.

Hyperinsulinemic-euglycemic clamp analysis was performed as described (46), with minor modifications. In brief, 5–7 days before the clamp, mice were anesthetized by intraperitoneal injection of sodium pentobarbital (80–100 mg/kg) and a catheter was inserted into the right internal jugular vein for infusion. The analysis was performed under nonstressful conditions with conscious mice that had been deprived of food overnight for 4 hours. [3-^{3}H]Glucose (NEN Life Science) was infused for 2 hours at a rate of 0.05 μCi/min before initiation of the clamp, and a blood sample was collected at the end of this period to estimate basal glucose turnover. After a bolus injection of [3-^{3}H]glucose (10 μCi) and the onset of subsequent continuous infusion of [3-^{3}H]glucose (0.1 μCi/min), a hyperinsulinemic-euglycemic clamp was applied for 120 minutes with continuous infusion of insulin at a rate of 2.5 mU/kg per minute. Plasma glucose concentration was monitored every 10 minutes, and 30% glucose was infused at a variable rate to maintain plasma glucose at basal concentrations. Blood samples were collected 80, 90, 100, 110, and 120 minutes after the onset of the clamp for determination of the plasma concentrations of [3-^{3}H]glucose and ^3H_2O. The rates of glucose disposal and hepatic glucose production were calculated as described (47).

Measurement of body temperature, locomotor activity, and oxygen consumption in mice. Mice were housed individually at 22° to 23°C in transparent plastic cages (31 × 20 × 13 cm) placed in a light-controlled (12-hour light/12-hour dark cycle; fluorescent light, 200–300 lux) monitoring chamber (40 × 33 × 33 cm) that was equipped with a radioreceiver of a telemetry system (RPC-1; Data Sciences International) for retrieval of body temperature (48). A temperature probe (TA10TA-F20; Data Sciences International) was introduced into the abdominal cavity of mice anesthetized with a mixture of halothane and O_2 (Fluothane; Takeda; 3%–4% for induction and 1% for maintenance). After recovery for more than 10 days, the mice were monitored for body temperature every 1 hour for 3 days. Locomotor activity was detected by passive (pyroelectric) infrared sensors (FA-05 F5B; Omron). Data were collected and analyzed with the use of a Chronobiology kit (Stanford Software Systems) (49). Oxygen consumption of mice in the fed condition was measured with an indirect calorimetric system every 6.5 minutes for 24 hours at 28°C as described previously (50). In brief, room air was pumped through an acrylic metabolic chamber, and the expired gas was filtered through thin cotton, dried, and subjected to gas analysis with an Alco System model RL-600 instrument. Energy expenditure was calculated as the product of the calorific value of oxygen (3.815 + [1.232 × respiratory quotient]) and the volume of O_2 consumed.

Immunoblot analysis. Total cell lysates were prepared with a lysis buffer containing 25 mM Tris-HCl (pH 7.4), 150 mM NaCl, 1 mM EDTA, 1% Triton X-100, 50 mM NaF, 10 mM sodium pyrophosphate, 1 mM sodium vanadate, and 1 mM PMSF. Tissue homogenates prepared in the same lysis buffer were rotated for 1 hour at 4°C, in the additional presence of 0.2% sarkosyl and 10% glycerol before analysis. Protein samples were subjected to immunoblot analysis with antibodies to FSP27, perilipin (Sigma-Aldrich), UCP-1 (51), COXIV (Molecular Probes), α-tubulin (Sigma-Aldrich), or β-actin (Sigma-Aldrich). Immune complexes were detected with HRP-conjugated secondary antibodies and enhanced chemiluminescence reagents (GE Healthcare). The polyclonal antibodies to FSP27 were generated by injection of rabbits with a synthetic peptide (CTEEEQPAKSSLL) corresponding to the COOH-terminal portion of mouse FSP27 or with a glutathione-*S*-transferase fusion protein of mouse FSP27 (amino acid residues 45–127) that was expressed in and purified from *Escherichia coli*. The antibodies generated in response to the fusion protein were purified by affinity chromatography with Hi-Trap NHS-activated columns (GE Healthcare) coupled with glutathione-*S*-transferase or the fusion protein.

Microscopic analyses. For light microscopy, the tissue was fixed with formalin, embedded in paraffin, sectioned at a thickness of 6 μm, and mounted on glass slides by standard procedures. The sections were stained with hematoxylin-eosin. For electron microscopy, tissue was fixed for at least 4 hours at 4°C with 2.5% glutaraldehyde in 0.1 M sodium cacodylate buffer and then cut into pieces of approximately 1 mm^3. The tissue fragments were then fixed with 1% osmium tetroxide in 0.2 M sodium cacodylate buffer, washed in the buffer alone, dehydrated with a series of alcohol solutions, and embedded in resin. After polymerization of the resin at 60°C for 48 hours, sections were cut with a microtome and observed with an electron microscope (JEM-1200EX; JEOL) (52).

For oil red O staining, cells were fixed for 1 hour at room temperature with 10% formalin in PBS, washed 3 times with distilled water, and then stained for 1 hour with filtered 0.5% oil red O in 60% isopropanol. After washing 3 times with distilled water, the cells were examined with a light microscope. For immunofluorescence microscopy, cells were washed twice with PBS, fixed for 20 minutes at room temperature with 4% formaldehyde in PBS, washed 3 times with PBS, permeabilized with 0.2% Triton X-100 for 5 minutes, and washed an additional 3 times with PBS. They were then incubated for 60 minutes with 2% BSA in PBS, before exposure for 60 minutes at room temperature to rabbit polyclonal antibodies to FSP27 or to perilipin (Sigma-Aldrich). The cells were washed 3 times with PBS and then incubated for 1 hour with Alexa Fluor 555–conjugated goat antibodies to rabbit IgG (Molecular Probes) as well as with Bodipy 493/503 (Molecular Probes) for staining of neutral lipid. Cover slips were applied to the slides with Fluoro Guard Antifade Reagent (Bio-Rad), and the cells were examined with a laser-scanning microscope (LSM5 PASCAL, version 3; Carl Zeiss).

Measurement of oxygen consumption in isolated adipocytes. Mice were anesthetized with ether and perfused, first with Ca^{2+}- and Mg^{2+}-free PBS containing 1 mM EDTA and heparin sodium (10 U/ml) and then with Krebs-Ringer bicarbonate HEPES buffer (KRBH, pH 7.4) containing collagenase (1 mg/ml), through a cannula inserted in an open-chest procedure into the left ventricle, with draining from the right atrium. BAT and inguinal WAT were then rapidly removed and placed in PBS. After the removal of extraneous tissue, the remaining adipose tissue was minced, and WAT or BAT from 3 mice was combined, transferred to an incubator, and incubated with slow shaking at 37°C in KRBH containing fatty acid–free BSA (10 mg/ml), 2.5 mM glucose, and collagenase (1 mg/ml). BAT was incubated for 30 minutes, with additional shaking by hand every 5 minutes, after which the mixture was passed through a 200-mm nylon filter and centrifuged at 200 *g* for 1 minute at room temperature. The floating adipocytes were collected. The pieces of BAT remaining on the nylon filter were incubated for an additional 30 minutes with the collagenase solution, and the released cells were collected and combined with the initial batch. The pieces of WAT were incubated for 1 hour, and the released cells were collected as for BAT. All adipocytes were washed 3 times with KRBH to eliminate collagenase and were counted with a Thoma's hemacytometer. The cells were diluted to a density of 1×10^5 to 5×10^5 cells/ml for BAT and 2×10^5 to 15×10^5 cells/ml for WAT with KRBH containing fatty acid–free BSA (40 mg/ml) and 2.7 mM glucose. The cell suspensions were maintained for 1 hour at room temperature before analysis.

Oxygen consumption by the isolated adipocytes was measured with a Clark-style oxygen electrode (782 2-Channel Oxygen System, version 1.0; Strathkelvin Instruments). The cell suspension (200 μl) was added to a magnetically stirred chamber set with a thermostat to 37°C and was adjusted to a final volume of 1 ml with KRBH containing fatty acid–free BSA (40 mg/ml) and 2.7 mM glucose. The chamber was closed, and the

cells were incubated for 5 minutes to determine the basal respiratory rate. CL316,243 (Sigma-Aldrich) was then injected to give a final concentration of 100 nM with a Hamilton syringe through a small hole in the cover of the chamber. Alternatively, after measurement of basal oxygen consumption rate, oligomycin, a specific inhibitor of mitochondrial ATP synthase, was added to a concentration of 0.1 mg/ml for measurement of respiration devoted to ATP production. Cyanide, an inhibitor of the mitochondrial respiratory chain, was next added at a concentration of 3 mM to estimate respiration associated with proton leak. Uncoupled respiration was calculated by subtracting the oxygen consumption devoted to ATP production from total mitochondrial oxygen consumption.

Measurement of glucose and FFA oxidation in isolated adipocytes. Glucose and FFA oxidation were measured as described previously (53), with some modifications. In brief, for measurement of glucose oxidation, isolated adipocytes (2×10^5 cells) were incubated in a polypropylene tube with 1 ml of KRBH (pH 7.4) containing 2 mM glucose, 2% BSA, and 0.5 μCi of [1-^{14}C]-D-glucose (52 mCi/mmol). For measurement of FFA oxidation, isolated adipocytes (2×10^5 cells) were washed twice with KRBH containing 2% BSA and were then incubated with 1 ml of the same solution containing 0.4 mM oleic acid and 1.0 μCi of [1-^{14}C]oleic acid (53 mCi/mmol). The cells were incubated for 3 hours at 37°C, after which 0.5 ml of 4 M H_2SO_4 was added to the tube, and the generated $^{14}CO_2$ was trapped by filter paper treated with hyamine hydroxide and measured by scintillation spectrometry.

Depletion of FSP27 or perilipin in HW adipocytes. Five days after the onset of induction of differentiation, HW adipocytes were washed twice with PBS, detached from the culture dish by exposure to 0.25% trypsin and collagenase (0.5 mg/ml) in PBS, and resuspended in PBS. The cells (~3×10^6) were then mixed with siRNA duplexes and subjected to electroporation with a Bio-Rad Gene Pulser II system at a setting of 0.18 kV and 0.975 μF. The FSP27 siRNA was targeted to the mRNA sequence 5′-GCACAAUCGUGGAGACAGAAGAAUA-3′. The perilipin siRNA was obtained from Invitrogen. Immediately after electroporation, the cells were mixed with fresh DMEM supplemented with 10% FBS, and 10 minutes later they were seeded onto culture plates. They were subjected to assays at the indicated times (see the legends for Figures 5 and 6) after electroporation.

Forced expression of FSP27 in COS cells and cultured adipocytes. The coding sequence of mouse FSP27 was subcloned into the pIRES2-DsRed2 vector (Clontech), and the resulting construct was introduced into COS cells with the use of the FuGENE 6 reagent (Roche). Cells were incubated with Bodipy 493/503 (for detection of lipid droplets) and Hoechst 33258 (for detection of nuclei) for 30 minutes at 37°C in a cell incubator. They were then washed twice with PBS, fixed for 20 minutes at room temperature with 4% formaldehyde in PBS, and washed 3 times with PBS. For quantitative analysis, images were acquired with an IN Cell Analyzer 1000 (GE Healthcare). The number of lipid droplets per nucleus and their mean area were then measured with the use of Developer Toolbox software. For the overexpression of mouse FSP27 tagged at its COOH-terminus with the Flag epitope in cultured HB2 and HW adipocytes, an Adenovirus Cre/loxP kit was used (Takara).

Statistics. Quantitative data are presented as mean ± SEM. Differences between groups were examined for statistical significance with 2-tailed Student's *t* test. A *P* value of less than 0.05 was considered statistically significant.

Acknowledgments

We thank H. Niwa (RIKEN Center for Developmental Biology, Kobe, Japan) for EB3/5 embryonic stem cells; S. Shigeta and R. Kumagai for technical assistance; and M.P. Czech (University of Massachusetts Medical School, Worcester, Massachusetts, USA) for helpful discussion. This work was supported by a grant for the Intellectual Cluster Formation Project from the Ministry of Education, Culture, Sports, Science, and Technology of Japan (MEXT) to M. Kasuga; a grant for the 21st Century COE Program "Center of Excellence for Signal Transduction Disease: Diabetes Mellitus as a Model" from MEXT to M. Kasuga; and a Grant-in-Aid for Creative Scientific Research from MEXT to M. Kasuga.

Received for publication September 28, 2007, and accepted in revised form May 21, 2008.

Address correspondence to: Masato Kasuga, Department of Internal Medicine, Division of Diabetes, Metabolism, and Endocrinology, Kobe University Graduate School of Medicine, 7-5-1 Kusunoki-cho, Chuo-ku, Kobe 650-0017, Japan. Phone: 81-78-382-5860; Fax: 81-78-382-2084; E-mail: kasuga@med.kobe-u.ac.jp.

1. Kahn, B.B., and Flier, J.S. 2000. Obesity and insulin resistance. *J. Clin. Invest.* **106**:473–481.
2. Unger, R.H. 2003. Weapons of lean body mass destruction: the role of ectopic lipids in the metabolic syndrome. *Endocrinology.* **144**:5159–5165.
3. Shulman, G.I. 2000. Cellular mechanisms of insulin resistance. *J. Clin. Invest.* **106**:171–176.
4. Rosen, E.D., and Spiegelman, B.M. 2006. Adipocytes as regulators of energy balance and glucose homeostasis. *Nature.* **444**:847–853.
5. Tauchi-Sato, K., Ozeki, S., Houjou, T., Taguchi, R., and Fujimoto, T. 2002. The surface of lipid droplets is a phospholipid monolayer with a unique fatty acid composition. *J. Biol. Chem.* **277**:44507–44512.
6. Zweytick, D., Athenstaedt, K., and Daum, G. 2000. Intracellular lipid particles of eukaryotic cells. *Biochim. Biophys. Acta.* **1469**:101–120.
7. Miura, S., et al. 2002. Functional conservation for lipid storage droplet association among perilipin, ADRP, and TIP47 (PAT)-related proteins in mammals, *Drosophila*, and *Dictyostelium*. *J. Biol. Chem.* **277**:32253–32257.
8. Wolins, N.E., Brasaemle, D.L., and Bickel, P.E. 2006. A proposed model of fat packaging by exchangeable lipid droplet proteins. *FEBS Lett.* **580**:5484–5491.
9. Murphy, D.J., and Vance, J. 1999. Mechanisms of lipid body formation. *Trends Biochem. Sci.* **24**:109–115.
10. Danesch, U., Hoeck, W., and Ringold, G.M. 1992. Cloning and transcriptional regulation of a novel adipocyte-specific gene, FSP27. CAAT-enhancer-binding protein (C/EBP) and C/EBP-like proteins interact with sequences required for differentiation-dependent expression. *J. Biol. Chem.* **267**:7185–7193.
11. Puri, V., et al. 2007. Fat specific protein 27: A novel lipid droplet protein that enhances triglyceride storage. *J. Biol. Chem.* **282**:34213–34218.
12. Tamori, Y., Masugi, J., Nishino, N., and Kasuga, M. 2002. Role of peroxisome proliferator-activated receptor-gamma in maintenance of the characteristics of mature 3T3-L1 adipocytes. *Diabetes.* **51**:2045–2055.
13. Brasaemle, D.L., Dolios, G., Shapiro, L., and Wang, R. 2004. Proteomic analysis of proteins associated with lipid droplets of basal and lipolytically stimulated 3T3-L1 adipocytes. *J. Biol. Chem.* **279**:46835–46842.
14. Lehmann, J.M., et al. 1995. An antidiabetic thiazolidinedione is a high affinity ligand for peroxisome proliferator-activated receptor γ (PPARγ). *J. Biol. Chem.* **270**:12953–12956.
15. Petruschke, T., and Hauner, H. 1993. Tumor necrosis factor-alpha prevents the differentiation of human adipocyte precursor cells and causes delipidation of newly developed fat cells. *J. Clin. Endocrinol. Metab.* **76**:742–747.
16. Irie, Y., et al. 1999. Immortal brown adipocytes from p53-knockout mice: differentiation and expression of uncoupling proteins. *Biochem. Biophys. Res. Commun.* **255**:221–225.
17. Evans, M.J., and Scarpulla, R.C. 1990. NRF-1: a trans-activator of nuclear-encoded respiratory genes in animal cells. *Genes Dev.* **4**:1023–1034.
18. Virbasius, J.V., and Scarpulla, R.C. 1994. Activation of the human mitochondrial transcription factor A gene by nuclear respiratory factors: a potential regulatory link between nuclear and mitochondrial gene expression in organelle biogenesis. *Proc. Natl. Acad. Sci. U. S. A.* **91**:1309–1313.
19. Uldry, M., et al. 2006. Complementary action of the PGC-1 coactivators in mitochondrial biogenesis and brown fat differentiation. *Cell Metab.* **3**:333–341.
20. Granneman, J.G., Li, P., Zhu, Z., and Lu, Y. 2005. Metabolic and cellular plasticity in white adipose tissue I: effects of β_3-adrenergic receptor activation. *Am. J. Physiol. Endocrinol. Metab.* **289**:E608–E616.
21. Himms-Hagen, J., et al. 2000. Multilocular fat cells in WAT of CL-316243-treated rats derive directly from white adipocytes. *Am. J. Physiol. Cell Physiol.* **279**:C670–C681.
22. Greenberg, A.S., et al. 1991. Perilipin, a major hormonally regulated adipocyte-specific phosphoprotein associated with the periphery of lipid storage droplets. *J. Biol. Chem.* **266**:11341–11346.
23. Servetnick, D.A., et al. 1995. Perilipins are associated with cholesteryl ester droplets in steroidogenic adrenal cortical and Leydig cells. *J. Biol. Chem.* **270**:16970–16973.
24. Brasaemle, D.L., et al. 2000. Perilipin A increases triacylglycerol storage by decreasing the rate of triacyl-

glycerol hydrolysis. *J. Biol. Chem.* **275**:38486–38493.
25. Martinez-Botas, J., et al. 2000. Absence of perilipin results in leanness and reverses obesity in Lepr (db/db) mice. *Nat. Genet.* **26**:474–479.
26. Tansey, J.T., et al. 2001. Perilipin ablation results in a lean mouse with aberrant adipocyte lipolysis, enhanced leptin production, and resistance to diet-induced obesity. *Proc. Natl. Acad. Sci. U. S. A.* **98**:6494–6499.
27. Cases, S., et al. 1998. Identification of a gene encoding an acyl CoA:diacylglycerol acyltransferase, a key enzyme in triacylglycerol synthesis. *Proc. Natl. Acad. Sci. U. S. A.* **95**:13018–13023.
28. Lardizabal, K.D., et al. 2001. DGAT2 is a new diacylglycerol acyltransferase gene family: purification, cloning, and expression in insect cells of two polypeptides from Mortierella ramanniana with diacylglycerol acyltransferase activity. *J. Biol. Chem.* **276**:38862–38869.
29. Cases, S., et al. 2001. Cloning of DGAT2, a second mammalian diacylglycerol acyltransferase, and related family members. *J. Biol. Chem.* **276**:38870–38876.
30. Ntambi, J.M., and Miyazaki, M. 2004. Regulation of stearoyl-CoA desaturases and role in metabolism. *Prog. Lipid Res.* **43**:91–104.
31. Coleman, R.A., and Lee, D.P. 2004. Enzymes of triacylglycerol synthesis and their regulation. *Prog. Lipid Res.* **43**:134–176.
32. Schweiger, M., et al. 2006. Adipose triglyceride lipase and hormone-sensitive lipase are the major enzymes in adipose tissue triacylglycerol catabolism. *J. Biol. Chem.* **281**:40236–40241.
33. Londos, C., Sztalryd, C., Tansey, J.T., and Kimmel, A.R. 2005. Role of PAT proteins in lipid metabolism. *Biochimie.* **87**:45–49.
34. Murphy, D.J. 2001. The biogenesis and functions of lipid bodies in animals, plants and microorganisms. *Prog. Lipid Res.* **40**:325–438.
35. Forman, B.M., Chen, J., and Evans, R.M. 1997. Hypolipidemic drugs, polyunsaturated fatty acids, and eicosanoids are ligands for peroxisome proliferator-activated receptors alpha and delta. *Proc. Natl. Acad. Sci. U. S. A.* **94**:4312–4317.
36. Bogacka, I., Ukropcova, B., McNeil, M., Gimble, J.M., and Smith, S.R. 2005. Structural and functional consequences of mitochondrial biogenesis in human adipocytes in vitro. *J. Clin. Endocrinol. Metab.* **90**:6650–6656.
37. Wang, Y.X., et al. 2003. Peroxisome-proliferator-activated receptor δ activates fat metabolism to prevent obesity. *Cell.* **113**:159–170.
38. Saha, P.K., Kojima, H., Martinez-Botas, J., Sunehag, A.L., and Chan, L. 2004. Metabolic adaptations in the absence of perilipin. *J. Biol. Chem.* **279**:35150–35158.
39. Castro-Chavez, F., et al. 2003. Coordinated upregulation of oxidative pathways and downregulation of lipid biosynthesis underlie obesity resistance in perilipin knockout mice: a microarray gene expression profile. *Diabetes.* **52**:2666–2674.
40. Inohara, N., Koseki, T., Chen, S., Wu, X., and Nunez, G. 1998. CIDE, a novel family of cell death activators with homology to the 45 kDa subunit of the DNA fragmentation factor. *EMBO J.* **17**:2526–2533.
41. Zhou, Z., et al. 2003. *Cidea*-deficient mice have lean phenotype and are resistant to obesity. *Nat. Genet.* **35**:49–56.
42. Li, J.Z., et al. 2007. Cideb regulates diet-induced obesity, liver steatosis and insulin sensitivity by controlling lipogenesis and fatty acid oxidation. *Diabetes.* **56**:2523–2540.
43. Nordström, E.A., et al. 2005. A human-specific role of cell death-inducing DFFA (DNA fragmentation factor-alpha)-like effector A (CIDEA) in adipocyte lipolysis and obesity. *Diabetes.* **54**:1726–1734.
44. Liang, L., Zhao, M., Xu, Z., Yokoyama, K.K., and Li, T. 2003. Molecular cloning and characterization of CIDE-3, a novel member of the cell-death-inducing DNA-fragmentation-factor (DFF45)-like effector family. *Biochem. J.* **370**:195–203.
45. Barazzoni, R., Short, K.R., and Nair, K.S. 2000. Effects of aging on mitochondrial DNA copy number and cytochrome *c* oxidase gene expression in rat skeletal muscle, liver, and heart. *J. Biol. Chem.* **275**:3343–3347.
46. Kanda, H., et al. 2006. MCP-1 contributes to macrophage infiltration into adipose tissue, insulin resistance, and hepatic steatosis in obesity. *J. Clin. Invest.* **116**:1494–1505.
47. Kim, J.K., Kotani, K., Ciaraldi, T.P., Henry, R.R., and Kahn, B.B. 2001. Glucose toxicity and the development of diabetes in mice with muscle-specific inactivation of GLUT4. *J. Clin. Invest.* **108**:153–160.
48. Mohri, T., et al. 2003. Alterations of circadian expressions of clock genes in Dahl salt-sensitive rats fed a high-salt diet. *Hypertension.* **42**:189–194.
49. Masubuchi, S., Kataoka, N., Sassone-Corsi, P., and Okamura, H. 2005. Mouse Period1 (mPER1) acts as a circadian adaptor to entrain the oscillator to environmental light/dark cycles by regulating mPER2 protein. *J. Neurosci.* **25**:4719–4724.
50. Ohnuki, K., Haramizu, S., Oki, K., Ishihara, K., and Fushiki, T. 2001. A single oral administration of conjugated linoleic acid enhanced energy metabolism in mice. *Lipids.* **36**:583–587.
51. Nagase, I., et al. 1996. Expression of uncoupling protein in skeletal muscle and white fat of obese mice treated with thermogenic beta 3-adrenergic agonist. *J. Clin. Invest.* **97**:2898–2904.
52. Kitazawa, S., and Kitazawa, R. 2006. In situ detection of specific gene expression during and immediately after transcription at electron microscopic level. *J. Struct. Biol.* **153**:64–72.
53. Vessal, M., Mishra, S., Moulik, S., and Murphy, L.J. 2006. Prohibitin attenuates insulin-stimulated glucose and fatty acid oxidation in adipose tissue by inhibition of pyruvate carboxylase. *FEBS J.* **273**:568–576.

Neuroscience Letters 441 (2008) 167–172

Contents lists available at ScienceDirect

Neuroscience Letters

journal homepage: www.elsevier.com/locate/neulet

Hydrogen therapy reduces apoptosis in neonatal hypoxia–ischemia rat model

Jianmei Cai[a,b,1], Zhimin Kang[a,1], Wen Wu Liu[a], Xu Luo[b], Sun Qiang[a], John H. Zhang[c], Shigeo Ohta[d], Xuejun Sun[a,*], Weigang Xu[a], Hengyi Tao[a], Runping Li[a]

[a] Department of Diving Medicine, Faculty of Naval Medicine, Second Military Medical University, Shanghai 200433, PR China
[b] Department of pathology, Qingdao Medical University, Shandong 266021, PR China
[c] Department of Neurosurgery, Loma Linda University, Loma Linda, California, USA
[d] Department of Biochemistry and Cell Biology, Institute of Development and Aging Sciences, Graduate School of Medicine, Nippon Medical School, 1-396 Kosugi-cho, Nakahara-ku, Kawasaki City 211-8533, Japan

ARTICLE INFO

Article history:
Received 24 April 2008
Received in revised form 20 May 2008
Accepted 20 May 2008

Keywords:
Hydrogen
Hydroxyl radical
Hypoxic ischemia
Apoptosis

ABSTRACT

Hypoxia–ischemia (HI) brain injury is a major cause of neuronal cell death especially apoptosis in the perinatal period. This study was designated to examine the effect of hydrogen therapy on apoptosis in an established neonatal HI rat pup model. Seven-day-old rat pups were subjected to left common carotid artery ligation and then 90 min hypoxia (8% oxygen at 37 °C). Immediately after HI insult, pups were placed into a chamber filled with 2% H_2 for 30 min, 60 min, or 120 min, respectively. 24 h after 2% H_2 therapy, the pups were decapitated and brain injury was assessed by 2,3,5-triphenyltetrazoliumchloride (TTC), Nissl, and TUNEL staining, as well as caspase-3, caspase-12 activities in the cortex and hippocampus. H_2 treatment in a duration-dependent manner significantly reduced the number of positive TUNEL cells and suppressed caspase-3 and -12 activities. These results indicated H_2 administration after HI appeared to provide brain protection via inhibition of neuronal apoptosis.

Hypoxia–ischemia (HI) insult is a relatively frequent occurrence in the perinatal period and can lead to neuron death [17]. In the complex factors involved in the neuronal death, reactive oxygen species (ROS) or reactive nitrogen species (RNS) such as the hydroxyl radical (•OH), superoxide anion (O_2^-), hydrogen dioxide (H_2O_2), nitric oxide (NO), peroxynitrite ($ONOO^-$), appear to play a critical role. The brain has potent defenses including dietary free-radical scavengers (ascorbate, α-tocopherol), the endogenous tripeptide glutathione, and enzymatic antioxidants against ROS. Although increased expression of these enzymes can occur in response to ischemia [6], endogenous antioxidant capacity can be overwhelmed after HI insult, leading to increased ROS concentrations. Excessive ROS can result in DNA fragment, lipid peroxidation, and inactivation of protein [9] leading to apoptosis or necrosis depending on the severity of oxidative stress. Among the ROS, OH and $ONOO^-$ are much more reactive and react indiscriminately with nucleic acids, lipids and proteins. Neuron membranes are rich in polyunsaturated fatty acids, and neonatal brain is more susceptible to oxidative damage [8]. There is not known detoxification system for •OH and $ONOO^-$; therefore, scavenging •OH and $ONOO^-$ is a critical antioxidant process [15].

HI injury to the brain has been shown to result in rapid cell death with features of both acute necrosis and delayed apoptotic cell death [11,13]. Apoptosis is a programmed cell death that is characterized by specific ultrastructural changes that include cell shrinkage, nuclear condensation and DNA fragmentation. At the molecular level, apoptosis is activated by the aspartate-specific cysteineprotease (caspase) cascade, including caspase-12 and -3. Caspase-12 is localized to the ER and specifically activated by ER stress, and caspase-3 is considered to be the most important of the executioner caspases and is activated by any of the initiator caspases [4].

Hydrogen gas has been used in medical applications to prevent decompression sickness (DCS) in deep divers for safety profiles [5]. Recently, Ohsawa et al. found that molecular hydrogen can selectively reduce •OH and $ONOO^-$ in cell-free systems and exert a therapeutic antioxidant activity, in a rat middle cerebral artery occlusion model [14]. But the mechanism involved in the protective effects of H_2 therapy was unclear. In this study, we examined whether H_2 therapy offers neuroprotection by reducing HI-induced caspase-dependent apoptosis.Seven-day-old Sprague–Dawley rat pups were randomly assigned to the following five groups: (1) control group (no carotid ligation, hypoxia) ($n = 20$), (2) HI group

* Corresponding author. Fax: +86 21 65492382.
E-mail address: sunxjk@hotmail.com (X. Sun).
[1] Both contributed equally to this work.

0304-3940/$ – see front matter © 2008 Elsevier Ireland Ltd. All rights reserved.
doi:10.1016/j.neulet.2008.05.077

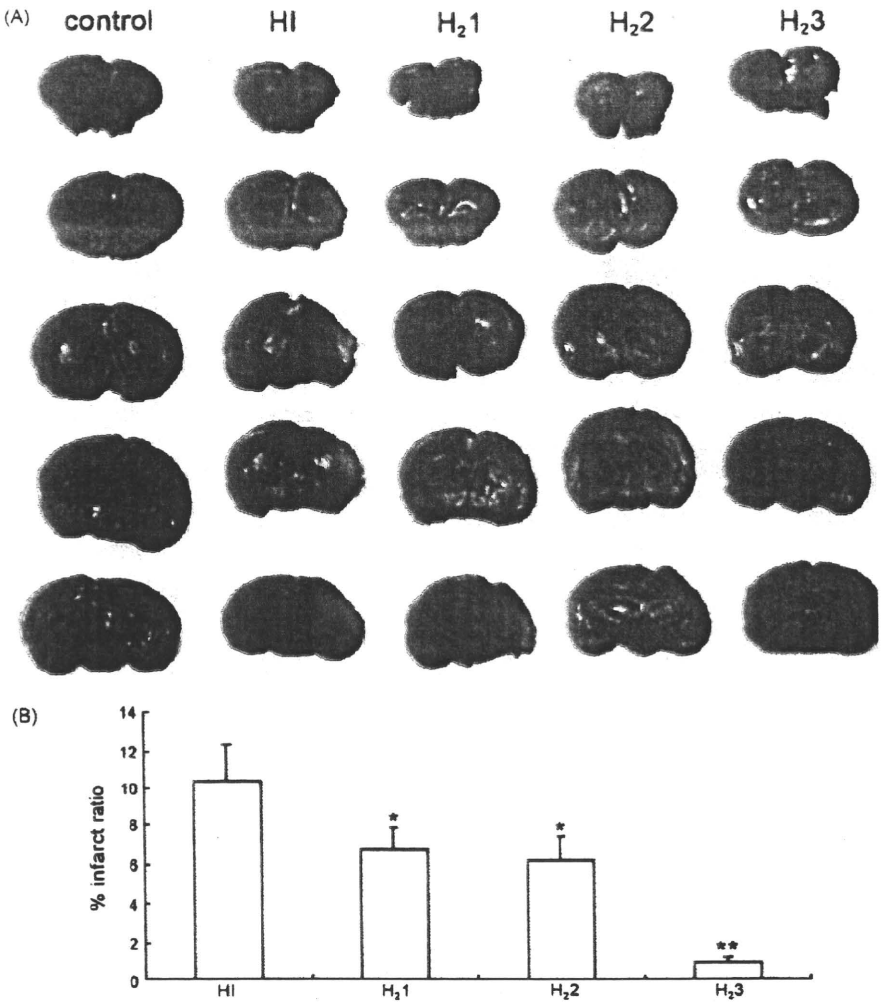

Fig. 1. TTC staining of damaged brains and infarct ratio. (A) Representative samples of TTC-stained coronal sections were derived from 8-day-old neonatal rats after H_2 therapy. Marked cerebral infarction was observed in the HI group. (B) Infarct ratio of each group. The infarct ratio was 10.4% in HI group, 6.77% in $H_2$1, 6.24% in $H_2$2 and 1.04% in $H_2$3 group. The results indicated that H_2 therapy decreased the volume of infarction, especially in $H_2$3 group.

(carotid ligation and hypoxia) (n = 60), (3) HI + $H_2$1 group (30 min 2% H_2 therapy) (n = 60), (4) HI + $H_2$2 group (60 min 2% H_2 therapy) (n = 60), (5) HI + $H_2$3 group (120 min 2% H_2 therapy) (n = 60). Each group was composed of pups from each litter to obtain parity within the groups. The Animal and Ethics Review Committee at the Second Military Medical University evaluated and approved the protocol used in this study.

The model used in this study was based on the Rice–Vannucci model [17]. Pups were housed with the dam under a 12:12 h light-dark cycle, with food and water available ad libitum throughout the studies. These neonatal rats were anesthetized by inhalation with diethyl ether. The rats were kept at a temperature of 37 °C as the left common carotid artery was exposed and ligated with 5–0 surgical sutures. After operation, the pups were returned to the holding container. Anesthesia and surgery time averaged 5 min per pup. Surgery was completed for an entire little, and the pups were allowed to recover with their dams for 1 h (for rehydration via nursing). Then they were placed in a jar perfused with a humidified gas mixture (8% oxygen balanced nitrogen) for 90 min. Both the jar and mixture were kept at 37 °C to maintain a constant thermal environment. All surviving pups were returned to their dams after hypoxia exposure.

The pups were placed into chamber (2% hydrogen; 1.0 atmosphere absolute, ATA) for 30 min, 60 min or 120 min immediately after HI insult. The chamber was flushed with mixed gases for 5 min to replace the air in the chamber. Continuous temperature monitoring was executed to avoid temperature changes. Fresh gas ventilation was maintained throughout treatments.

24 h after 2% H_2 therapy, the pups were decapitated and the left brain hemispheric volumes were measured. Briefly, the brains were quickly removed after decapitation and placed in cold saline for 5 min, cut at 2-mm intervals from the frontal pole into 5 coronal sections. After incubated in 1% 2,3,5-triphenyltetrazolium chloride (TTC) for 8 min at 37 °C, the brain slices were fixed in 4% formalin for 24 h. The volumes of each of the sections were summed by an image analysis system (ImageJ, a public domain image analysis program, developed at the National Institutes of Health). The percentage of infarction (infarct ratio) was calculated by dividing the infarct volume by the total volume of the slices.

For Nissl staining, the 4-μm sections were hydrated in 1% toluidine blue at 50 °C for 20 min. After rinsing with double distilled water, they were dehydrated and mounted with permount. The cortex and the CA1 area of hippocampus from each animal were

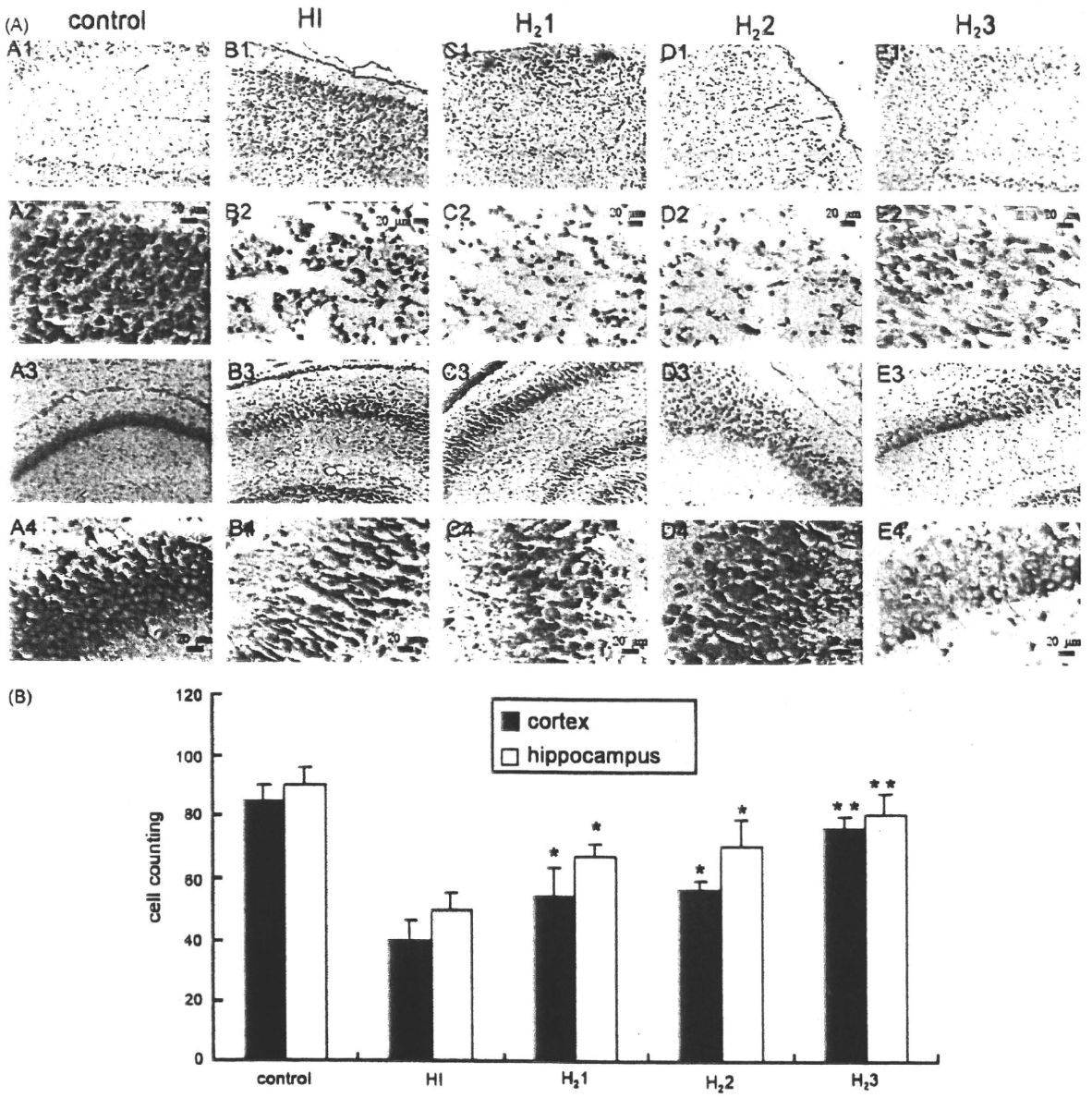

Fig. 2. Nissl staining of damaged cortex (A1-E2) and hippocampus (A3-E4) and cell counting. (A) Nissl staining. Cortex and hippocampus in each group after H_2 therapy are shown at two different magnifications (A1-E1, A3-E3: ×10, A2-E2, A4-E4: ×40). More neuronal loss and dead cells appeared in the HI group after injury. In CA1 sector of control and $H_2$3 group, the cell outline was clear and the structure was compact. Cells were big and have abundant cytoplasm and Nissl body. In HI group, cells arranged sparsely and the cell outline was fuzzy. The cells with eumorphism were significantly reduced. (B) Cell counting. The number of Nissl staining cells in cortex and hippocampus of HI group was lower than that of $H_2$1, $H_2$2 ($P < 0.05$) and $H_2$3 groups ($P < 0.01$).

captured and Imaging-Pro-Plus (LEIKA DMLB) was used to perform quantitative analysis of cell numbers.

TUNEL staining was performed on paraffin-embedded sections by using the in situ cell death detection kit (Roche). According to standard protocols, the sections were dewaxed and rehydrated by heating the slides at 60 °C. Then these sections were incubated in a 20 μg/ml proteinase K working solution for 15 min at room temperature. The slides were rinsed three times with PBS before they were incubated in TUNEL reaction mixture for 1 h at 37 °C. Dried area around sample and added Converter-AP on samples for 1 h at 37 °C. After rinsing with PBS (5 min, three times), sections were colourated in dark with nitroblue tetrazolium (NBT) and 5-bromo-4-chloro-3-indolylphosphate (BCIP).

Six visual fields (0.6 mm^2) of the cerebral cortex and CA1 were photographed in each section. The number of staining cells in each field was counted at higher magnification (×40). The data were represented as the number of cells per high-power field.

Brain samples from the cortex and hippocampus were taken from the impaired hemispheres of neonatal rats at 24 h after H_2 administration. The activities of caspase-3 and -12 were measured with caspase-3/CPP32 Fluorometric Assay Kit and caspase-12/CPP32 Fluorometric Assay Kit (BIOVISION Research Products 980 Linda Vista Avenue, Mountain View, CA 94043 USA).

Briefly, brain samples were homogenized in ice-cold cell lysis buffer and kept at 4 °C for 1 h. Brain homogenate was centrifuged (Eppendorf, 5810R) at 12,000 × *g* for 15 min at 4 °C. The supernatant

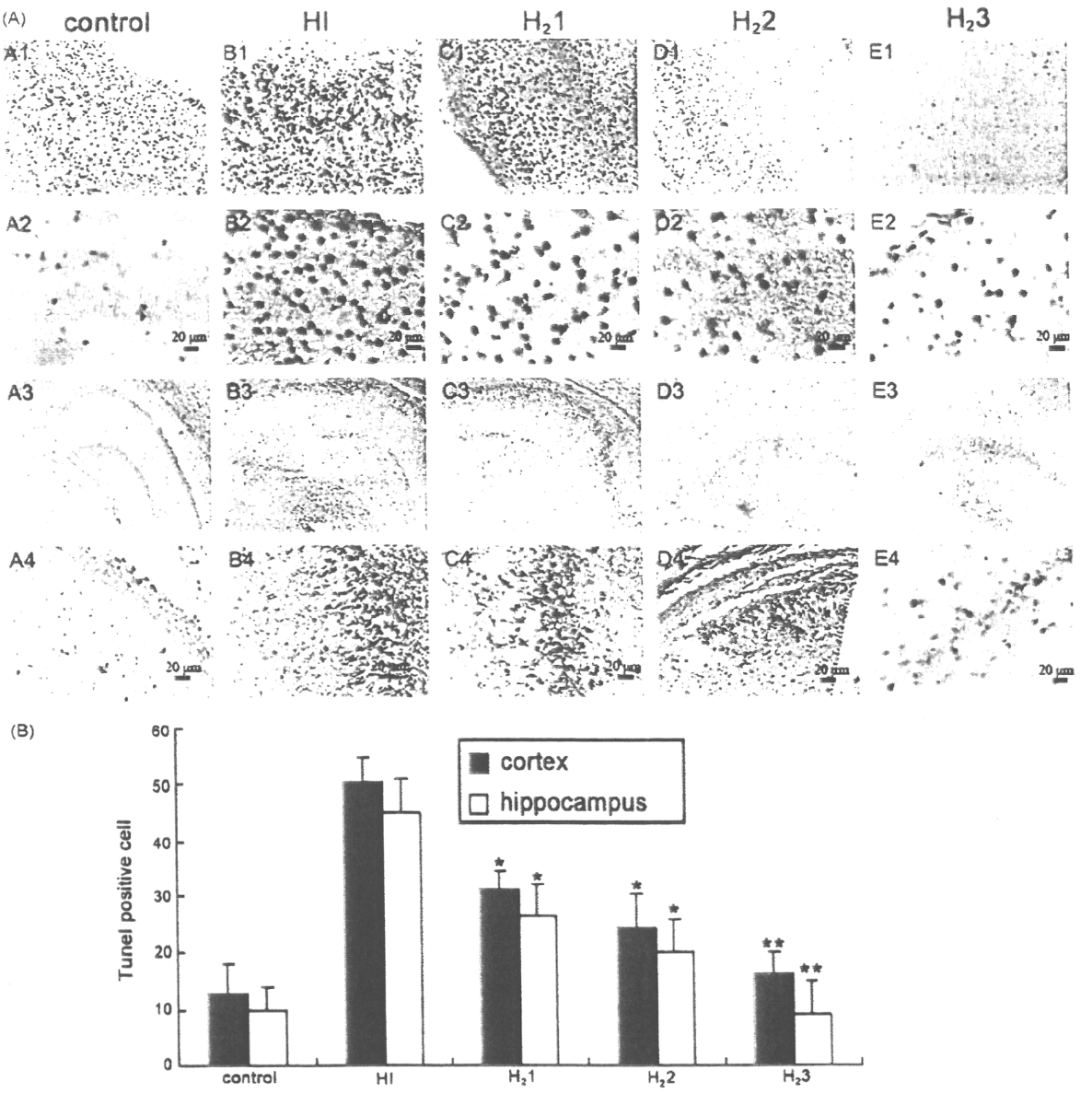

Fig. 3. TUNEL staining of damaged cortex (A1-E2) and hippocampus (A3-E4) and TUNEL-positive cell counting. (A) TUNEL staining. Cortex and hippocampus in each group after H_2 administration are shown at two different magnifications (A1-E1, A3-E3: ×10, A2-E2, A4-E4: ×40). The TUNEL-positive material was localized in the nuclei of the neurons. In samples collected from the HI group, the damaged cells were characterized by a round and shrunken morphology. The processes disappeared and the neuronal body became rounded with strong TUNEL staining in the nucleus. An occasional TUNEL-positive cell was found in control and $H_2$3 group. (B) Cell counting. The cortex and hippocampus of HI group had a higher proportion of TUNEL-positive cells than that of $H_2$1, $H_2$2 ($P<0.05$) and $H_2$3 groups ($P<0.01$). H_2 therapy reduced the number of TUNEL-positive cells, and prevented neurons from apoptosis after HI.

was removed and stored at −80 °C until use. Protein content was measured by using the Enhanced BCA Protein Assay Kit. 20–200 μg cell lysates were incubated in a 96-well plate with 2 × Reaction Buffer (50 μl). The reaction was started by adding 1 mM DEVD–APC substrate (5 μl). After incubation in the dark at 37 °C, the plate was read in a fluorometer equipped with a 400-nm excitation filter and 505-nm emission filter.

All quantitative data are expressed as mean ± S.D. The significance of differences between means was verified by ANOVA followed by Tukey test. For analyzing the results of cell counting, a non-parametric Kruskal–Wallis ANOVA was used followed by Dunn's test. $P<0.05$ was considered significant.

Fig. 1 shows representative photographs of TTC-stained sections from rat pups in each group, at 24 h after 2% H_2 therapy. The infarct ratio in HI group (10.4%) was markedly higher than that in $H_2$1 group (6.77%, 30 min 2% H_2), $H_2$2 group (6.24%, 60 min 2% H_2) and $H_2$3 group (1.04%, 120 min 2% H_2). The results indicated that H_2 therapy dramatically decreased the volume of infarction, especially in $H_2$3 group. However, there was not significantly different in infarct ratio between $H_2$1 group and $H_2$2 group.

Fig. 2 shows representative samples of Nissl staining from the cerebral cortex and hippocampus of pups at 24 h after 2% H_2 therapy. Extensive neuronal changes in the cortex and CA1 sector of the hippocampus were noticed with features of considerable dark,

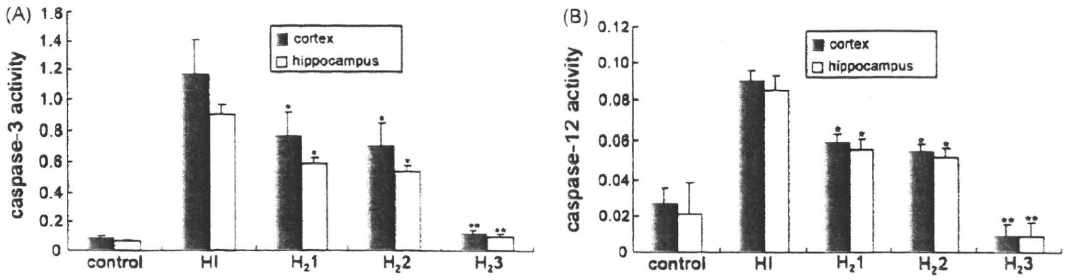

Fig. 4. The activities of caspase-3 (A) and -12 (B) in the impaired cortex and hippocampus. After H_2 therapy, the activities of caspase-3 and -12 were dramatically reduced after HI insult. The activity of caspase-12 in $H_2$3 group was lower than that in control group, while the activity of caspase-3 in $H_2$3 group was higher than that in control group. A single administration of 2% H_2 reduced apotosis after HI insult via suppressing the activities of caspase-3 and -12.

pyknotic neurons in HI group (B1–4). More Nissl-stained cells (E1–4) were observed in $H_2$3 group than that in HI group ($P < 0.01$).

Fig. 3 shows that TUNEL-positive cells were significantly increased in cortex and hippocampus of HI group (B1, B3). 120 min 2% H_2 therapy markedly reduced the number of TUNEL-positive cells (E1, E3). At higher magnification, the nuclei of cells were clearly stained in both hippocampus and cortex (B2, B4, E2, E4). A few TUNEL-positive cells were identified in samples from normal control pups (A1-4). And there was no difference in cell counting between $H_2$1 and $H_2$2 group.

The activities of caspase-3 and -12 were measured at 24 h after HI insult as shown in Fig. 4. The activity of caspase-3 was 1.17 ± 0.23 in cortex and 0.9 ± 0.06 in hippocampus in HI group. 120 min 2% H_2 administration significantly reduced the activity of caspase-3 in the cortex (0.117 ± 0.02) and hippocampus (0.09 ± 0.16) ($P < 0.01$ vs. HI). Similarly, higher caspase-12 activity was obtained in cortex and hippocampus in HI group which was reduced by 2% H_2 treatment ($P < 0.01$ vs. $H_2$3).

In this study, 2% H_2 administration immediately after HI insult significantly reduced the infarct ratio, in a duration-dependent manner. This result is consistent with the observation by Ohsawa et al. [14] in adult focal ischemia. The protective effects of H_2 on HI brain injury seem related to its anti-apoptotic actions because hydrogen increased the number of survival neurons, decreased the number of apoptotic cells, and reduced the activities of caspase-3 and -12. These observations indicate a single and short term 2% H_2 administration may have clinical potentials in the management of HI brain injury in neonates. We are not aware that hydrogen was used previously as a therapy either in animal models of neonatal brain injury or in clinical practice.

The brain consumes a large quantity of oxygen, making it particularly susceptible to oxidative stress [10]. Oxidative stress is a major contributor to ischemic brain injury especially in neonatal brain [2]. An excellent antioxidant for clinical intervention should be easily available, permeable into cytoplasm or nucleus, and without toxicity. Hydrogen is one of the most plentiful gases in the universe. The two most common methods for producing hydrogen are steam reforming and electrolysis (water splitting). It has been established that some algae and bacteria produce hydrogen [3]. Hydrogen molecule is electronically neutral and is expected to easily penetrate the cellular and intracellular membranes. It is oxidized into water in the body which is not harmful to cells. Hydrogen does not disturb metabolic oxidation–reduction reactions nor does it disrupt ROS involved in cell signaling [14]. As a physiological inert gas, hydrogen is less narcotic than nitrogen, and nitrogen easily develops bubbles than hydrogen in the decompression [1]. Therefore, H_2 has been used for deep diving for the above mentioned safety consideration.

Ohsawa et al. found that molecular hydrogen can selectively reduce $^{\bullet}OH$ and $ONOO^-$ in vitro and exert a therapeutic antioxidant activity in a rat middle cerebral artery occlusion model [14]. $^{\bullet}OH$ and $ONOO^-$ are the strongest oxidants and react indiscriminately with nucleic acids, lipids and proteins resulting in DNA fragment, lipid peroxidation, and inactivation of protein. O_2^- and H_2O_2 are detoxified by antioxidant defense enzymes, superoxide dismutase, and peroxidase or glutathione-peroxidase, respectively; however, no enzyme detoxifies $^{\bullet}OH$ and $ONOO^-$. Therefore, the ability of hydrogen to reduce or eliminate $^{\bullet}OH$ and $ONOO^-$ may be responsible for the neuroprotective effect especially anti-apoptotic effect observed in this study.

The reason we studied the activity of caspase-12 is that procaspase-12 is predominantly localized at the endoplasmic reticulum (ER) and is specifically activated by disturbances to ER homeostasis such as ER stress and mobilization of intracellular calcium ion store [12]. Studies have shown that the change of Ca^{2+} influx, efflux, release from intracellular Ca^{2+} stores and Ca^{2+} buffering contribute to the HI-induced Ca^{2+} ion disturbances [18]. Elevated intracellular calcium may activate calpain, a noncaspase protease, and induce the translocation of calpain from the cytosol to the membrane [16] where it may cleave procaspase-12 resulting in caspase-12 activation. Then caspase-12 activated caspase-3 which leads to apoptosis [7]. Hydrogen application reduced the activities of caspase-12 and -3 in this study. Apparently hydrogen therapy by quenching free-radicals may inhibit a variety of pathways that lead to caspase-3 activation which may involve caspase-12 and -9.

Hydrogen's neuroprotective effect is time dependent in this study. While the infarct volume was not significantly different between $H_2$1 group (30 min hydrogen) and $H_2$2 group (60 min hydrogen), much less infarction was observed in the $H_2$3 group (120 min hydrogen). Similar morphological observations was obtained in Nissl staining that more Nissl positive cells were observed in $H_2$3 group than that in HI group. In TUNEL staining, again, 120 min 2% H_2 therapy markedly reduced the number of TUNEL-positive cells, while there was no difference in cell counting between $H_2$1 and $H_2$2 group. Finally, only 120 min 2% H_2 administration significantly reduced the activity of caspase-3 and -12.

We conclude that given the easiness of administrating of hydrogen and the safety of 2% hydrogen, hydrogen may be a good candidate in the management of HI brain injury as a safe and effective antioxidant with minimal side effects.

References

[1] A.O. Brubakk, T.S. Neuman, Physiology and Medicine of Diving, 5th ed., Saunders, London, 2003.
[2] J.W. Calvert, J.H. Zhang, Pathophysiology of a hypoxic-ischemic insult during the perinatal period, Neurol. Res. 27 (2005) 246–260.
[3] D. Das, T.N. Veziroglu, Hydrogen production by biological processes: a survey of literature, Int. J. Hydrogen Energ. 26 (2001) 13–28.
[4] S. Elmore, Apoptosis: a review of programmed cell death, Toxicol. Pathol. 35 (2007) 495–516.

[5] P. Fontanari, M. Badier, C. Guillot, C. Tomei, H. Burnet, B. Gardette, Y. Jammes, Changes in maximal performance of inspiratory and skeletal muscles during and after the 7.1-MPa Hydra 10 record human dive, Eur. J. Appl. Physiol. 81 (2000) 325–328.
[6] S. Fukui, T. Ookawara, H. Nawashiro, K. Suzuki, K. Shima, Post-ischemic transcriptional and translational responses of EC-SOD in mouse brain and serum, Free Rad. Biol. Med. 32 (2002) 289–298.
[7] J. Hitomi, T. Katayama, M. Taniguchi, A. Honda, K. Imaizumi, M. Tohyama, Apoptosis induced by endoplasmic reticulum stress depends on activation of caspase-3 via caspase-12, Neurosci. Lett. 357 (2004) 127–130.
[8] T. Ikeda, Y.X. Xia, M. Kaneko, H. Sameshima, T. Ikenoue, Effect of the free radical scavenger, 3-methyl-1-phenyl-2-pyrazolin-5-one (MCI-186), on hypoxia–ischemia-induced brain injury in neonatal rats, Neurosci. Lett. 329 (2002) 33–36.
[9] S. Kuroda, B.K. Siesjö, Reperfusion damage following focal ischemia: pathophysiology and therapeutic windows, Clin. Neurosci. 4 (1997) 199–212.
[10] S. Love, Oxidative stress in brain ischemia, Brain Pathol. 9 (1999) 119–131.
[11] L.J. Martin, M.E. Blue, M.V. Johnston, Apoptosis has a prolonged role in the neurodegeneration after hypoxic ischemia in the newborn rat, J. Neurosci. 20 (2000) 7994–8004.
[12] T. Nakagawa, H. Zhu, N. Morishima, E. Li, J. Xu, B.A. Yankner, J. Yuan, Caspase-12 mediates endoplasmic-reticulum-specific apoptosis and cytotoxicity by amyloid β, Nature 403 (2000) 98–103.
[13] F.J. Northington, D.M. Ferriero, D.L. Flock, L.J. Martin, Delayed neurodegeneration in neonatal rat thalamus after hypoxia–ischemia is apoptosis, J. Neurosci. 21 (2001) 1931–1938.
[14] I. Ohsawa, M. Ishikawa, K. Takahashi, M. Watanabe, K. Nishimaki, K. Yamagata, K. Katsura, Y. Katayama, S. Asoh, S. Ohta, Hydrogen acts as a therapeutic antioxidant by selectively reducing cytotoxic oxygen radicals, Nat. Med. 13 (2007) 688–694.
[15] S.S. Sheu, D. Nauduri, M.W. Anders, Targeting antioxidants to mitochondria: a new therapeutic direction, Biochim. Biophys. Acta 1762 (2006) 256–265.
[16] K. Suzuki, S. Imajoh, Y. Emori, H. Kawasaki, Y. Minami, S. Ohno, Calcium-activated neutral protease and its endogenous inhibitor. Activation at the cell membrane and biological function, FEBS Lett. 220 (1987) 271–277.
[17] R.C. Vannucci, J.R. Connor, D.T. Mauger, C. Palmer, M.B. Smith, J. Towfighi, S.J. Vannucci, Rat model of perinatal hypoxic-ischemic brain damage, J. Neurosci. Res. 55 (1999) 158–163.
[18] H. Yao, G.G. Haddad, Calcium and pH homeostasis in neurons during hypoxia and ischemia, Cell Calcium 36 (2004) 247–255.

Neurobiology of Disease

Age-Dependent Neurodegeneration Accompanying Memory Loss in Transgenic Mice Defective in Mitochondrial Aldehyde Dehydrogenase 2 Activity

Ikuroh Ohsawa,[1,2] Kiyomi Nishimaki,[1] Yayoi Murakami,[1] Yuko Suzuki,[1] Masahiro Ishikawa,[1] and Shigeo Ohta[1]

[1]Department of Biochemistry and Cell Biology and [2]The Center of Molecular Hydrogen Medicine, Institute of Development and Aging Sciences, Graduate School of Medicine, Nippon Medical School, Kawasaki 211-8533, Japan

Oxidative stress may underlie age-dependent memory loss and cognitive decline. Toxic aldehydes, including 4-hydroxy-2-nonenal (HNE), an end product of lipid peroxides, are known to accumulate in the brain in neurodegenerative disease. We have previously shown that mitochondrial aldehyde dehydrogenase 2 (ALDH2) detoxifies HNE by oxidizing its aldehyde group. To investigate the role of such toxic aldehydes, we produced transgenic mice, which expressed a dominant-negative form of ALDH2 in the brain. The mice had decreased ability to detoxify HNE in their cortical neurons and accelerated accumulation of HNE in the brain. Consequently, their lifespan was shortened and age-dependent neurodegeneration and hyperphosphorylation of tau were observed. Object recognition and Morris water maze tests revealed that the onset of cognitive impairment correlated with the degeneration, which was further accelerated by APOE (apolipoprotein E) knock-out; therefore, the accumulation of toxic aldehydes is by itself critical in the progression of neurodegenerative disease, which could be suppressed by ALDH2.

Key words: ALDH2; HNE; memory loss; mitochondria; oxidative stress; transgenic mice

Introduction

A decline in cognitive function is associated with aging, mainly as a result of oxidative stress in the brain (Mattson, 2004). Reactive oxygen species (ROS), strong oxidizing molecules including hydroxyl radicals, modify proteins, nucleic acids, and polyunsaturated fatty acids of the lipid membrane, and injure cells. Lipid peroxidation leads to the formation of highly reactive α,β-unsaturated aldehydes, primarily malondialdehyde and 4-hydroxy-2-nonenal (HNE) (Schneider et al., 2001). In particular, HNE is a strong electrophile and has the ability to readily adduct and damage proteins (Uchida, 2003). The accumulation of HNE-adducted proteins in pyramidal neurons has been observed in the brains of patients with Alzheimer's disease (AD) and Parkinson's disease (Yoritaka et al., 1996; Lovell et al., 1997; Montine et al., 1997; Sayre et al., 1997). HNE application *in vitro* mimics the pathological changes noted in AD, including modification of tau (Takeda et al., 2000; Liu et al., 2005) and β-amyloid (Murray et al., 2007), inhibition of the glucose transporter (Reagan et al., 2000), and microtubular disruption (Gadoni et al., 1993), and eventually leads to cell death (Mark et al., 1997).

HNE is adducted with glutathione via glutathione *S*-transferase (Xie et al., 1998), oxidized by aldehyde dehydrogenase (ALDH) to form 4-hydroxy-2-noneoate (Tjalkens et al., 1999), or reduced by aldo-keto reductase, alcohol dehydrogenase (ADH) or amyloid β-peptide-binding ADH (ABAD) to form 1,4-dihydroxynonene (Srivastava et al., 1998; Murakami et al., 2008). These multiple pathways are used to detoxify HNE in cells (Siems and Grune, 2003). We found previously that mitochondrial ALDH2-deficient neuronal cells exhibited increased vulnerability to HNE (Ohsawa et al., 2003a). The cells accumulated HNE and showed decreased resistance to oxidative insult, suggesting that ALDH2 functions as a protector against oxidative stress by oxidizing HNE. However, ALDH2 is well known to oxidize acetaldehyde produced from ethanol into acetate (Higuchi et al., 2004). A mutant allele, *ALDH2*2*, has a single point mutation (G→A) in exon 12 of the active *ALDH2*1* gene and is confined to Asians. This mutation results in a substitution of glutamate 487 to lysine (E487K), acting in a dominant-negative manner (Bosron and Li, 1986). Individuals with the *ALDH2*2* allele exhibit the alcohol-flushing syndrome attributable to an elevated blood acetaldehyde level.

We reported previously that a molecular epidemiological analysis revealed a higher concentration of lipid peroxides (LPOs) in the sera of ALDH2-deficient females than in those carrying an active ALDH2 (Ohsawa et al., 2003b), and that ALDH2 deficiency is a risk factor for late-onset AD, synergistically acting with the $\varepsilon4$ allele of the apolipoprotein E gene (*APOE-ε4*) (Kamino et al., 2000). This finding was recently confirmed by studies in China and Korea (Jo et al., 2007; Wang et al., 2008). To verify the role of ALDH2-deficiency in age-associated

Received Nov. 5, 2007; revised May 2, 2008; accepted May 4, 2008.

This work was supported by grants from the Ministry of Health, Labour and Welfare (Longevity Science, H17-Chouju-009; Nervous and Mental Disorders, 17A-10) (S.O.).

Correspondence should be addressed to Shigeo Ohta, Department of Biochemistry and Cell Biology, Institute of Development and Aging Sciences, Graduate School of Medicine, Nippon Medical School, 1-396 Kosugi-cho, Nakahara-ku, Kawasaki 211-8533, Japan. E-mail: ohta@nms.ac.jp.

DOI:10.1523/JNEUROSCI.4956-07.2008

 0270-6474/08/286239-11$15.00/0

neurodegenerative diseases, we examined physiological changes, and learning and memory impairments by using transgenic (Tg) mice expressing ALDH2*2 in the brain. Here, we show that ALDH2-deficient mice present with age-dependent signs of neurodegeneration such as loss of pyramidal cells, activation of glial cells, and prominent deficits in cognition.

Materials and Methods

Transgenic mice. To generate Tg mice that express ALDH2*2, a transgene containing a mouse version of *ALDH2*2* under the control of the human elongation factor-1α (EF1α) promoter was constructed. A DNA fragment containing *ALDH2*2* in plasmid pBluescript SK (Ohsawa et al., 2003a) was digested with *Xba*I and inserted into the *Xba*I site of plasmid pEF1-BOS (Mizushima and Nagata, 1990). The 4.2 kb *Apa*LI–*Pvu*I fragment of EF1α promoter-*ALDH2*2* derived from the resultant plasmid was purified and dissolved in TE buffer at a concentration of 3 μg/ml. Tg mice were produced in accordance with a standard procedure. In brief, the DNA fragment was microinjected into 800 fertilized eggs taken from superovulated C57BL/6 females. The injected eggs were surgically transferred to the oviducts of C57BL/6 pseudopregnant females to produce male chimeric mice. Sixteen mice carrying the transgene were selected by PCR of tail DNA with primers 5′-NNTCTAGAGCCACCATGGCT-CAGGGCGCCCATA and 5′-GAAGGGTTGACGGTGGGAAATGTT. F_1 heterozygous animals were backcrossed to C57BL/6 mice for more than five generations, and homozygous mice (*ALDH2*2*$^{+/+}$) were finally obtained. Next, three independent lines (DAL101, DAL102, and DAL103) were selected according to the expression of *ALDH2*2* in the brain determined by the following method. Poly(A)$^+$ RNA was extracted from the brain and mismatch reverse transcription (RT)-PCR was performed with *ALDH2*-specific primers 5′-AGATGTCAGGGAGTGG-CAGG (see Fig. 1, primer A) and 5′-GTGGCACTTTGACAGTAA-CCGTCTTAACGT (see Fig. 1, primer B). The amplified cDNA fragment was incubated with *Acl*I and subjected to PAGE. Two digested fragments (54 and 30 bp) were derived from exogenous *ALDH2*2*, whereas the fragment not digested with *Acl*I (84 bp) was from endogenous *ALDH2*. To quantify the expression of *ALDH2* and *ALDH2*2* transcripts in each region of the brain, their cDNA was qualified by ABI7700 with real-time RT-PCR primers and probe 5′-ACCTGTCCCAAGCTCTGCAG, 5′-GGAGACTGGGCCCCAAAC, and 5′-CTGGCACTGTGTGGATC-AACTGCTACG for endogenous *ALDH2*, and 5′-AAAACC-CAACAAGATATACTGAGAAAAAC, 5′-GACCTGATACTCTCA-AGGGTCCC, and 5′-CACTGTCTAGAGTGAGGGTCCCCACCTG for exogenous *ALDH2*2*. DAL101 was further mated with *ApoE*$^{-/-}$ mice (purchased from Taconic Farms) and offspring carrying the genotype *ALDH2*2*$^{+/+}$*/ApoE*$^{-/-}$ were obtained.

All mice were kept on a 12 h light/dark cycle with *ad libitum* access to food and water. The studies were approved by the Animal Care and Use Committee of Nippon Medical School. All experiments were performed by examiners blinded to the genotypes or treatments of the mice.

Primary culture of neurons. Primary cultures of cortical neurons were prepared from 17 d mouse embryos by the method described previously (Ohsawa et al., 2007). In brief, neocortical tissue was cleaned of meninges, minced, and treated with trypsin. After mechanical dissociation by pipetting, cells were resuspended in DMEM (Invitrogen) supplemented with insulin (5 μg/ml), transferrin (5 μg/ml), putrescine (100 μM), selenium (5 ng/ml), and penicillin–streptomycin, and then plated onto poly-L-lysine-coated plates at a density of 5×10^4 cells/cm^2. After 3 d of the culture, we used neurons for analysis of cell viability. For preparing hippocampal cells, hippocampus of 17 d mouse embryo was cleaned of meninges, minced, and treated with protease mixture (SUMILON). After mechanical dissociation by pipetting, we resuspended cells in nerve cell culture medium (SUMILON), and then plated onto poly-L-lysine-coated plates at a density of 5×10^4 cells/cm^2, changed one-half of the medium once every 2 d, and then used neurons at day 1 and day 9 for analysis of neurite outgrowth and cell viability, respectively. Neuronal identity was confirmed by immunostaining with the neuron marker anti-TUJ-1 (Covance) and/or anti-MAP2 (Sigma-Aldrich) and astrocyte marker anti-glial fibrillary acidic protein (GFAP) (ThermoImmunon) antibodies. After incubation with BODIPY FL goat anti-mouse IgG (Invitrogen), cells were imaged by confocal scanning microscopy (Olympus) using excitation and emission filters of 488 and 510 nm, respectively. Preparations containing >90% neurons were used for experiments. Apoptosis was detected by DNA strand breaks using terminal deoxynucleotidyl transferase-mediated biotinylated UTP nick end-labeling (TUNEL) according to the procedure of the manufacturers (MBL).

Preliminary observation and neurological reflexes. Mice were first observed in their home cages for general activity and levels of aggression. Each mouse was then observed in a bare cage for general health, presence of whiskers, and appearance of fur. Mice were challenged to evaluate reflex responses including eye blink, ear twitch, whisker touch, and righting reflexes (Miyakawa et al., 2001).

Open-field test. Locomotor activity was measured using an open-field apparatus (45 × 45 × 65 cm) (Kim et al., 2006). Animals were placed in the center of the apparatus in standard indoor-lighting conditions and total distance traveled for 10 min was recorded. Between sessions, the apparatus was wiped clean with 70% ethanol.

Wire hanging test. The neuromuscular strength was tested by the wire hanging test (Hamann et al., 2003). In brief, mice were placed on a wire netting, which was lightly shaken, causing the mouse to grip the wire. After a 5 s cutoff time, the wire netting was turned upside down (180°) and the latency to fall was recorded for the maximum time.

Immunohistochemistry. The brain was removed and left one was kept at −80°C for biochemical assay. The right brain was further fixed for 4 h at room temperature by using 4% paraformaldehyde in PBS and subsequently cryoprotected with 30% sucrose in PBS. Frozen brain was sectioned at 8 μm thickness using a cryostat (Leica), mounted on slides, and air-dried. To stain sections with antibodies against NeuN (clone A60; Millipore), GFAP, and phospho-Tau (clone AT8; Pierce), the M.O.M. kit (Vector Laboratories) was used by the method according to the manufacturer. For double staining with anti-NeuN, antimonoclonal antibody and rabbit anti-GFAP polyclonal antibody (Abcam), we used Texas Red goat anti-mouse IgG (Invitrogen) and BODIPY FL goat anti-rabbit IgG (Invitrogen) as secondary antibodies and visualized signals with a laser-scanning confocal microscope.

Immunoblot analysis. The left hippocampus was dissected and Dounce-homogenized in cold lysate buffer [10 mM Tris, pH 7.4, 320 mM sucrose, 1% Triton X-100, 1% CHAPS (3-[(3-cholamidopropyl)-dimethylammonio]-1-propanesulfonate), 0.025% NaN_3, 1 mM EDTA, 1 mM EGTA, 50 mM sodium fluoride, 2 mM sodium orthovanadate, and protease inhibitor Complete tablets EDTA-free (Roche)] and stored at −80°C. Protein concentration was determined with the BCA protein assay kit (Pierce). Equal amounts of protein (100 μg) were separated on 10–20% polyacrylamide gels (Daiichi), transferred onto PolyScreen transfer membranes (PerkinElmer), and incubated in blocking buffer consisting of TBS (10 mM Tris, pH 7.6, and 150 mM NaCl) with 5% bovine serum albumin. For immunodetection of specific bands on the blots, Can Get Signal immunoreaction enhancer solution (Toyobo) was used by the method according to the manufacturer. Blots were incubated with primary antibodies to tau phospho-Ser-202/205 (AT-8; 1:500; Pierce), pan-tau (TAU-5; 1:1000; Millipore), p35 and p25 C terminus (C-19; 1:200; Santa Cruz), and cyclin-dependent kinase 5 (Cdk5) (C-8; 1:100; Santa Cruz) and further incubated with alkaline phosphatase-conjugated secondary antibodies (1:10,000; Cappel). Signals were visualized with AttoPhos substrate (Roche). Blots were stripped with stripping buffer (62.5 mM Tris, pH 6.8, 100 mM 2-mercaptoethanol, 2% SDS) and reprobed with antibody to β-actin (1:10,000; Sigma-Aldrich) to normalizing the amounts of loaded proteins.

HNE concentration. Concentration of HNE in the brain was determined using a colorimetric assay kit (HAE-586; OXIS International) according to the manufacturer's instructions. The protein concentration of each sample was measured using a BCA protein assay reagent (Pierce).

Visual object recognition test. The visual object recognition test (vORT) was used to test recognition memory (Wang et al., 2004). Mice were first habituated in a 25 × 40 cm cage for 6 h before training. During 10 min of training, two plastic blocks with different shapes and colors were presented. Object recognition was scored by the number of approaches to

and/or sniffs of the object and was reported as percentage preference (recognition index). One day after training, one of the conditioned blocks was replaced with a novel object to test for memory retention, and recognition index was scored during 5 min of testing.

Water maze test. The apparatus used for water maze tasks was a circular pool (1.5 m diameter) painted white and filled with water maintained at 25°C, and rendered opaque by the addition of nontoxic white paint. The maze is located in a room containing several simple visual, extramaze cues. Mice were trained in the morning to swim to a 10-cm-diameter circular clear acryl resin platform submerged 1 cm beneath the surface of the water and invisible to the mice while swimming. Mice were monitored by a camera mounted above the pool, and all trials were stored on PC for subsequent analysis. In each trial, the mouse was placed and released into the pool at one of four designated start points in a pseudorandom order and allowed to find and escape to the submerged platform and remain there for 20 s. If a mouse failed to find the platform within 60 s, it was guided carefully to the platform and allowed to remain there for 20 s. After this, each mouse was dried gently with a towel and placed into a holding cage for 30 min until the start of next trial. Mice were given four trials a day for 5 d. Retention of the spatial training was assessed 1 h after the last training trial. A single probe trial consisted of a 60 s free swim in the pool without the platform. Mice were placed and released at the location opposite the site where the platform had been located and the time spent in each quadrant was recorded. Finally, after the probe trial, a visible platform was placed in the training quadrant 1 cm above the surface of the water. As in the place-learning task, the escape latencies were measured during at least four trials per session except that the test was conducted in a single day.

Statistical analysis. We performed statistical analyses using StatView software (SAS Institute) by applying an unpaired two-tailed Student's *t* test and ANOVA followed by Fisher's exact test for single and multiple comparisons, respectively. To calculate survival curves, the Kaplan–Meier method was used and the survival periods were compared with the log rank test (Mantel–Cox) for univariate analysis. We performed experiments for quantification in a blinded manner.

Results

Expression of ALDH2*2 in the brain and vulnerability of ALDH2*2-expressing neurons to HNE

The mouse version of the dominant-negative form of ALDH2 (ALDH2*2) was introduced under an EF1α promoter (Fig. 1*A*), which constitutively expresses genes in most tissues (Wakabayashi-Ito and Nagata, 1994). Because the expression extent depends on the location inserted, we paid attention to the expression of ALDH2*2 in the brain and selected three independent transgenic founders (DAL101, DAL102, and DAL103) and confirmed expression of ALDH2*2 by RT-PCR in the brain (Fig. 1*B*). One founder (DAL101), which expressed the highest amount of ALDH2*2, was maintained as homozygotes and mainly used for additional experiments. The amount of exogenous ALDH2*2 transcripts relative to endogenous ALDH2 transcripts was higher in the olfactory bulb, cortex, hippocampus, and midbrain in DAL101 (Fig. 1*C*).

To evaluate the effect of ALDH2*2 in neurons, we examined the ability of HNE detoxification and found that exposure to HNE resulted in a more rapid decrease of viable cells in the ALDH2*2-expressing neurons. At first, hippocampal neurons were prepared from embryonic 17 d DAL101. Moderate neuritogenesis was seen after 1 d in culture. Then, cells were treated with HNE and incubated for an additional 1 d. Immunostaining with anti-MAP2 antibody showed that neurite length of neurons prepared from DAL101 was shorter than that from non-Tg control (CTL) mice (C57BL/6) (Fig. 2*A*,*B*). After 9 d in culture, when a mature synaptic network was established, the hippocampal neurons were treated with HNE and further incubated for 1 d. Immunostaining with anti-MAP2 antibody revealed that the MAP2-positive neurites derived from DAL101 mice were decreased by the treatment with 3 μM HNE (Fig. 2*C*,*D*). Additionally, apoptosis was more induced by the treatment with HNE in neurons derived from DAL101 mice (Fig. 2*E*,*F*). Furthermore, cortical neurons were prepared from embryonic 17 d DAL101 and cultured for 3 d. Twenty-four hours after treatment with 1 μM HNE, 77.1% of ALDH2*2-expressing neurons were injured and detached from the dish, whereas control neurons prepared from CTL mice were attached and showed normal morphology with neuron-specific TUJ-1-positive neurites (Fig. 2*G*). The sensitivity of ALDH2*2-expressing neurons to HNE was dose-dependent (Fig. 2*H*). At that time, a higher amount of HNE was accumulated in ALDH2*2-expressing neurons (Fig. 2*I*), indicating that the metabolism ability of exogenous HNE decreased. These findings clearly show that the decline of ALDH2 activity makes neurons less resistant to HNE.

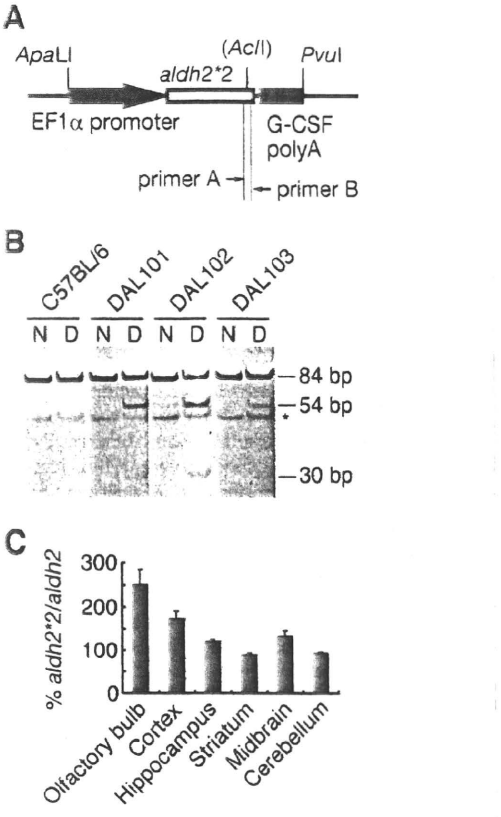

Figure 1. Generation of DAL mice. ***A***, Schematic drawing of the transfected DNA fragment. DAL mice were generated by the injection of 4.2 kb *ApaLI–PvuI* fragment into fertilized eggs. ***B***, RT-PCR analysis revealed that three transgenic founders expressed exogenous *ALDH2*2* in the brain. For PCR, primers shown in ***A*** were used (see Materials and Methods). The obtained PCR fragments (N) were digested with *AclI* (D). Two short fragments (54 and 30 bp) were derived from exogenous *ALDH2*2*, whereas the nondigested fragment was from endogenous *ALDH2*. *Nonspecific bands. ***C***, In the brain of DAL101, real-time RT-PCR analysis revealed more exogenous *ALDH2*2* transcripts relative to endogenous *ALDH2* transcripts in the olfactory bulb, cortex, hippocampus, and midbrain. Data are mean ± SEM ($n = 4$).

Accumulation of HNE in the brain is accelerated and lifespan is shortened

To clarify the relationship of ALDH2*2-expressing neurons with HNE, we measured HNE in the brain and found that a higher amount of HNE was accumulated in the brain of old DAL mice